



저작자표시-비영리-변경금지 2.0 대한민국

이용자는 아래의 조건을 따르는 경우에 한하여 자유롭게

- 이 저작물을 복제, 배포, 전송, 전시, 공연 및 방송할 수 있습니다.

다음과 같은 조건을 따라야 합니다:



저작자표시. 귀하는 원저작자를 표시하여야 합니다.



비영리. 귀하는 이 저작물을 영리 목적으로 이용할 수 없습니다.



변경금지. 귀하는 이 저작물을 개작, 변형 또는 가공할 수 없습니다.

- 귀하는, 이 저작물의 재이용이나 배포의 경우, 이 저작물에 적용된 이용허락조건을 명확하게 나타내어야 합니다.
- 저작권자로부터 별도의 허가를 받으면 이러한 조건들은 적용되지 않습니다.

저작권법에 따른 이용자의 권리는 위의 내용에 의하여 영향을 받지 않습니다.

이것은 [이용허락규약\(Legal Code\)](#)을 이해하기 쉽게 요약한 것입니다.

[Disclaimer](#)

공학석사 학위논문

**Quantitative Flow Characterization of
Homogeneous and Isotropic Turbulence
using Stereoscopic Particle Image
Velocimetry**

Stereo-PIV 를 이용한 균질한 등방성 난류의
유동 특성에 관한 정량적 연구

2020 년 2 월

서울대학교 대학원

기계항공공학부

정 현 균

Quantitative flow characterization of homogeneous and isotropic turbulence using stereoscopic particle image velocimetry

Stereo-PIV 를 이용한 균질한 등방성 난류의
유동 특성에 관한 정량적 연구

지도교수 황 원 태

이 논문을 공학석사 학위논문으로 제출함
2019 년 10 월

서울대학교 대학원
기계항공공학부
정 현 균

정현균의 공학석사 학위논문을 인준함
2019 년 12 월

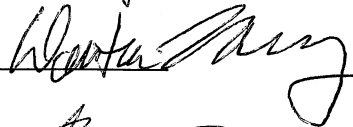
위 원 장

김 호 영



부위원장

황 원 태



위 원

박 형 민



Abstract

Quantitative flow characterization of homogeneous and isotropic turbulence using stereoscopic particle image velocimetry

Hyunkyun Jung

Department of Mechanical and Aerospace Engineering
The Graduate School
Seoul National University

We herein conduct a wide range of quantitative analysis on homogeneous and isotropic turbulence (HIT) by means of statistical flow characterization. A turbulence chamber with synthetic jet actuators achieves experimental realization of homogeneity and isotropy without mean flow: Re_λ up to 228. Stereoscopic particle image velocimetry is employed to measure velocity fields of full three-components. One-point statistics confirm the high quality of stationary HIT, while two-point statistics including velocity correlation function, structure function, and energy spectrum demonstrate scale-to-scale isotropy and the similarity in the inertial subrange. The dissipation rate is measured using five different methods, aiming at comparing their performance and examining their applicability to general PIV experiments with insufficient spatiotemporal resolution. We crosscheck the measurement performance and show that the methods relying on Kolmogorov's similarity hypothesis provide consistent results whereas large-eddy method and direct method return underestimated results due to excessive and limited spatial resolution, respectively.

Keyword: *homogeneous isotropic turbulence, turbulence statistics, dissipation rate measurement, stereoscopic particle image velocimetry*

Student Number: 2018-27421

Table of Contents

Abstract	i
Table of Contents	ii
List of Tables	iv
List of Figures	v
Nomenclature	viii
1. Introduction	1
2. Experimental Setup	4
2.1 Turbulence chamber	4
2.2 Stereoscopic particle image velocimetry	5
3. One-point Statistics and Flow Quality	9
3.1 Statistically stationary turbulence	9
3.2 Evaluation of flow quality	10
4. Two-Point Statistics and Flow Scale	21
4.1 Velocity correlation function	21
4.2 Second-order structure function	22
4.3 Energy spectrum	24
5. Measurement of Dissipation Rate	33
5.1 Direct method	33
5.2 Structure-function fitting method	35
5.3 Energy spectrum fitting method	36
5.4 Dissipation scaling method	37

5.5 Large-eddy method	38
5.6 Comparison	41
6. Uncertainty Analysis	53
6.1 Literature survey	53
6.2 Error correction	56
6.3 Uncertainty propagation	61
6.4 Numerical verification	65
6.5 Results and discussion	68
7. Concluding Remarks	80
Bibliography	81
Abstract in Korean	88

List of Tables

2.1 Experimental conditions	7
2.2 PIV interrogation conditions	7
3.1 Statistical moments of velocity fluctuations (case 1)	14
3.2 Statistical moments of velocity derivatives (case 1)	18
4.1 Estimated integral length scales and ratios	29

List of Figures

2.1 Stereo-PIV measurement of HIT chamber	8
2.2 Mean jet exit velocity according to the amplifier intensity for the subwoofer speakers	8
3.1 Independent samples taken from a statistical ensemble	12
3.2 Example flow field (case 1): vector map for in-plane velocity and color map for out-of-plane velocity (a) Instantaneous velocity field (b) Mean velocity field from 2,000 samples; Note that the reference scale is expanded by three-times	13
3.3 Probability density functions of velocity fluctuations (case 1)...	15
3.4 Homogeneity plot (a) Map of $\frac{k(x_1, x_2)}{\langle k \rangle}$ (case 1): 95% values in 0.939-1.066 (b) Homogeneity quantities in other conditions; the intervals show the range that contains 95% values	16
3.5 Isotropy plot (a) Map of $\frac{u_{2,RMS}(x_1, x_2)}{u_{1,RMS}(x_1, x_2)}$ (case 1): 95% values in 0.829-1.082 (b) Isotropy quantities in other conditions and in other directions; the intervals show the range that contains 95% value ..	17
3.6 Probability density functions of velocity derivatives (case 1): longitudinal derivatives in solid lines and transverse derivatives in dashed lines	19
3.7 Turbulent kinetic energy (TKE) for each case (a) TKE varying with the woofer amplification level (b) TKE variation with the jet exit velocity, showing a more linear correlation	20
4.1 Velocity correlation functions (case 1, 3, 5) (a) Longitudinal velocity correlation functions (b) Transverse velocity correlation functions plotted against the isotropy relation	27
4.2 Procedure to obtain the extrapolated longitudinal velocity correlation	

function (case 1, horizontal velocities) (a) Exponential regression in the logarithmic graph (b) Full velocity correlation function including the extrapolated data	28
4.3 Second-order structure functions (case 1, 3, 5) for two different directions (a) Longitudinal structure functions (b) Transverse structure functions	30
4.4 One-dimensional energy spectra (case 1) (a) Longitudinal 1D energy spectra using two different methods (b) Longitudinal and transverse 1D energy spectra	31
4.5 Radial two-dimensional energy spectra (case 1)	32
5.1 Compensated structure functions and the estimated dissipation rate values (case 1-5) (a) Compensated longitudinal SFs (horizontal velocities) (b) Compensated transverse SFs (horizontal velocities)	43
5.2 Dissipation rate measurement using structure-function fitting method, five points corresponding to case 1 to 5 (a) Dissipation rate from four SFs in the four different directions (b) Averaged quantities over the four values for each condition	44
5.3 Dissipation rate measurement using energy spectra fitting method, five points corresponding to case 1 to 5	45
5.4 Normalized longitudinal 1D energy spectra (case 1 to 5)	46
5.5 Dissipation rate measurement using dissipation scaling method, five points corresponding to case 1 to 5	47
5.6 Schematic diagram of the large-eddy method adopting a SGS model from large-eddy simulations (LES)	48
5.7 Dissipation rate measurement using large eddy method, five points corresponding to case 1 to 5; Inner box is the normalized PIV resolution (Δ_{IW} over η)	49
5.8 Probability density functions of the dissipation rate measured using the large-eddy method (case 1), showing lognormal distribution ...	50

5.9 Comparison of the dissipation rate measurement using five different methods, five points corresponding to case 1 to 5; Inner box is the normalized PIV resolution (Δ_{IW} over η)	51
5.10 Repeatability check for the five methods (for case 1), errorbar corresponds to the 95% confidence interval	52
6.1 Flow chart of Monte-Carlo method using the PIV model with a DNS dataset	73
6.2 Convergence of Monte-Carlo results for the mean corrected dissipation rate ($N_{\text{frame}} = 100$, $\Delta_{IW} = 32$, 50% overlap)	74
6.3 Comparison of analytical estimation and Monte-Carlo results for 95% uncertainty value ($N_{\text{frame}} = 100$, $\Delta_{IW} = 32$, 50% overlap, (32 nd , 8 th) sub-window) (a) velocity fluctuation RMS (b) strain rate invariant squared (c) dissipation rate	75
6.4 Histogram of relative error between approximate solution and Monte-Carlo results for dissipation rate mean value ($N_{\text{frame}} = 100$, $\Delta_{IW} = 32$, 50% overlap, $N_t = 1,000$) (a) $\xi = 10\%$ (b) $\xi = 20\%$	76
6.5 Comparison of analytical estimation and Monte-Carlo results for 95% uncertainty value ($N_{\text{frame}} = 100$, $\Delta_{IW} = 32$, 50% overlap, (32 nd , 8 th) sub-window) (a) velocity fluctuation RMS (b) strain rate invariant squared (c) dissipation rate	77
6.6 Comparison of corrected and non-corrected results for mean value ($N_{\text{frame}} = 100$, $\Delta_{IW} = 32$, 50% overlap, (32 nd , 8 th) sub-window) (a) velocity fluctuation RMS (b) strain rate invariant squared (c) dissipation rate	78
6.7 Correction to the PIV dissipation rate measurement ($N_{\text{frame}} = 100$) (a) $\Delta_{IW} = 32$, 50% overlap, $y = 8$ (b) $\Delta_{IW} = 64$, 50% overlap, $y = 18$	79

Nomenclature

Roman Symbols

C_1	Kolmogorov constant for 1D energy spectrum (0.53)
C_2	Kolmogorov constant for 2 nd -order structure function (2.12)
C_κ	Kolmogorov constant for 3D energy spectrum (1.64)
C_s	Smagorinsky constant
C_ε	Normalized dissipation constant
$D_{LL}(r)$	Longitudinal second-order structure function
$D_{TT}(r)$	Transverse second-order structure function
$E[]$	Expectation value
$E_{ii}(k_j)$	One-dimensional energy spectrum
$E_{ii}(k)$	Radial two-dimensional energy spectrum
$F(r)$	Longitudinal velocity correlation function
$G(r)$	Transverse velocity correlation function
K	Kurtosis (fourth standardized moment)
L_{ii}	Integral length scale
N	Sample number (image pair)
Re_λ	Taylor microscale Reynolds number
S	Skewness (third standardized moment)
$ S $	Strain rate invariant $(2S_{ij}S_{ij})^{1/2}$
S_{ij}	Strain rate tensor
$U[]$	Uncertainty value
U_i	Mean velocity
e	Random error in PIV measurement
k	Turbulent kinetic energy
	Two-dimensional wavenumber
k_α	One-dimensional wavenumber
u_i	Fluctuating component of velocity (u_i')
$u_{i,RMS}$	Root-mean-square of velocity fluctuation
$u_{i,meas}$	Velocity that is directly measured by SPIV

Greek Symbols

Δ_{IW}	Size of PIV interrogation window
---------------	----------------------------------

Δ_{sheet}	Laser sheet thickness in the PIV model
Δt	Time-interval of PIV image pair
Δx	Vector spacing of PIV measurement
	Displacement measurement from a PIV interrogation
Π	Large-scale energy transfer rate
α	Camera angle of Scheimpflug condition
ε	Dissipation rate of turbulent kinetic energy
ε_{LE}	Dissipation rate measured by the large-eddy method
η	Kolmogorov length scale
θ	Lens angle of Scheimpflug condition
λ	Taylor microscale
μ	Dynamic viscosity ($\rho\nu$)
ν	Kinematic viscosity
ζ	Uncertainty ratio
ρ	Density of fluid
τ_{ij}	Viscous stress tensor

Abbreviations

CI	Confidence interval
DNS	Direct numerical simulation
FFT	Fast Fourier transform
HIT	Homogeneous and isotropic turbulence
IR	Inertial subrange
IW	(PIV) Interrogation window
LES	Large-eddy simulation
MCM	Monte-Carlo method
PDF	Probability density function
PIV	Particle image velocimetry
RMS	Root-mean-square
SF	Structure-function
SGS	Sub-grid scale
SPIV	Stereoscopic particle image velocimetry
TKE	Turbulent kinetic energy (k)
TSM	Taylor-series method

Chapter 1. Introduction

Turbulence is an everyday phenomenon, which can be readily observed in nature and technology. The respiratory airflow through the larynx is turbulent, as is the natural convection in the room where you sit. In the open air, fallen leaves rustle in the turbulent wind and pollutants disperse with turbulent convection. At a larger scale, flow motions in the atmospheric and oceanic circulation are turbulent. It is also prevalent in industrial applications such as the aerodynamic drag on vehicles, the reacting flows in internal combustion engines, and heat exchangers. This ubiquitous nature of turbulence makes the study of turbulence important and intriguing.

Under suitable conditions, which generally come to one requirement that the kinematic viscosity ν of the fluid is sufficiently small compared to the flow scale, the fluid velocity at any given time and position takes random values and is not determined by large-scale boundary conditions themselves. These fluctuating motions are referred to as turbulence. Since turbulent flow shows irregular patterns with unstable motion, it is complicated to analyze and predict the chaotic flow motion. Therefore, we hereby consider the simplest type of turbulence, namely homogeneous and isotropic turbulence (HIT). Turbulence is said to be homogeneous and isotropic if all the statistical moments of fluctuating motions are invariant under any translation or rotation. HIT can be described by one statistical state that is independent of initial and boundary conditions, as the flow field of steady HIT is boundless in time and space (Batchelor, 1953).

From the theoretical point of view, HIT is attractive because such a simplified study is essential for obtaining concrete theoretical results for the more general cases

of turbulence (Monin & Yaglom, 1971). Since Taylor (1935) introduced the concept of HIT and its statistical descriptions, many theoreticians such as von Karman and Howarth (1937) have developed more general kinematics and dynamics of HIT. In particular, Kolmogorov (1941a) provided a monumental theory that describes the universal structure of turbulence using the framework of homogeneity and isotropy in the statistical distribution of the small-scale turbulent motions. Kolmogorov's similarity hypotheses asserted that the statistical properties of the turbulence at some small-scales are uniquely determined by the dissipation rate ε , which suggests that the rate of viscous dissipation of turbulent energy is one of the most important characteristics of turbulence.

For experimentalists, HIT is considered to be idealistic in the sense that the exact realization of such motion is highly challenging, and that the theory is mainly based on abstract reasoning rather than empirical observations. Thus, many experimental researchers have attempted to create real HIT in the laboratory to accomplish the purpose of understanding actual turbulent phenomena. The most common way of generating turbulence in the laboratory is the wind tunnel, where a steady flow passes through a grid and develops into turbulent flow (Comte-Bellot & Corrsin, 1966). These turbulent flows show two-dimensional homogeneity and isotropy, but streamwise inhomogeneity and anisotropy due to the decay of turbulence along the tunnel. Accordingly, many laboratory devices such as stirring tanks using oscillating grids (Desilva & Fernando, 1994; Ott & Mann, 2000), rotating facilities (Douady *et al.*, 1991; Liu *et al.*, 1999; Friedman & Katz, 2002) or planar jet arrays (Variano *et al.*, 2004; Bellani & Variano, 2014; Carter *et al.*, 2016) were invented to minimize the mean flow. Despite their axisymmetric and stationary motion, they still exhibit anisotropy along an axis with a certain amount of mean flow and mean strain.

Spherical symmetry, on which HIT theory assumes, can be attained by symmetric forcing from the corners of a regular polyhedron. Hwang and Eaton (2004) designed a very effective type of “turbulence chamber” to generate spherically symmetric HIT using synthetic jet actuators at the eight corners of a cubical acrylic box, and this type of configuration has since then been replicated by many other similar laboratory apparatuses (Goepfert *et al.*, 2010; Zimmermann *et al.*, 2010; Chang *et al.*, 2012; Dou *et al.*, 2016). This design results in outstanding homogeneity and isotropy with a high Reynolds number, such that realization of HIT with clear scale separation is accomplished. Moreover, it has turbulent motion with nearly zero mean flow and zero mean strain, which eliminates large-scale inhomogeneity and enables both Lagrangian and Eulerian measurements of turbulent motions.

In this study, we replicated the turbulence chamber with spherical symmetry using eight synthetic jet actuators to create HIT at five different intensities, and quantitatively characterized the turbulence. The turbulent flow characteristics including homogeneity, isotropy, and zero-mean flow are quantified using one-point statistics. Then, we analyze two-point statistics to quantify flow scales and monitor the scale-to-scale isotropy. For this purpose, velocity correlation functions, second-order structure-functions, and energy spectra are calculated. Accordingly, we measure the dissipation rate, which is a primary parameter in describing the turbulent flow, using five different methods: dissipation rate scaling, structure-function fitting, energy spectral fitting, large eddy method, and direct method. By crosschecking these methods, we can understand the advantages and limitations of each technique. Using the measured dissipation rate, the length- and time-scales of turbulence are quantified, and the universal structure of small-scale turbulence in HIT theory is confirmed.

Chapter 2. Experimental Setup

2.1. Turbulence chamber

The turbulence chamber is a cubical acrylic box, with length of 380 mm, and the eight corners cut off to make the inner side approximately spherical. It has detachable glass windows on each of the four lateral faces to provide optical access for the cameras and laser sheet. The chamber is shown in Figure 2.1. The synthetic actuators were mounted on the corners, pointing to the center of the chamber and generating symmetric turbulent flow at the center region. The synthetic jet is advantageous in that it creates a flow with net momentum flux but no net mass flux, and that it needs no external fluid source. Here, the working fluid is air. Subwoofer speakers with polypropylene cones (made by Peerless, rated power 50W, frequency response at 60-5,000 Hz) pushed air out of the plenum through round orifices (dia. 19mm). The discharged air jets passed through ejector tubes (dia. 40 mm, length 74 mm), which allowed the entrainment of air from the ports (21 mm × 10 mm) at the base, thereby increasing the flow rate. The steel grids at the tube end broke up the large scale structure from each synthetic jet, resulting in a mix of turbulence structures at the center of the chamber.

The subwoofer speakers were driven with sinusoidal waves amplified by two audio amplifiers (made by Behringer, 300 W for four channels, amplification level up to 28dB). The waves were created with an analog voltage output module (NI-9264, made by National Instrument), and each wave was independently set to randomly change the frequency (90-110 Hz) and phase ten times a second. Cosine taper function was applied at the conjunction part of the two sine waves at different phases, to eliminate signal discontinuity. The randomness prevented the formation

of any periodic structure, such as a standing wave that can possibly disturb the turbulence. We conducted measurement of five cases with different woofer amplification levels, which are presented in Table 2.1. To quantify the jet intensity of each case that is highly correlated with the overall turbulence intensity, we measured the jet velocities at the jet exit using hot-wire anemometer for twenty seconds for each of the eight jet actuators, and the mean values are shown in Figure 2.2.

2.2. Stereoscopic particle image velocimetry

Stereoscopic particle image velocimetry (SPIV) was applied to measure full three-components of velocity, which has been a useful technique for turbulent flow field measurements (van Doorne & Westerweel, 2007). The imaging domain (region of interest; ROI) was a planar region of $37 \times 37 \text{ mm}^2$. Two monotone CCD cameras (made by Vieworks, 12bit depth, $2048 \times 2048 \text{ px}^2$, $7.4 \mu\text{m}$ pixel array) was used with two Nikon 105 mm macro lenses at $f/2.8$. Scheimpflug mounts were installed to make the focal plane aligned with the planar domain (Prasad & Jensen, 1995). The lens angle θ was 20° each, and the camera angle α was 7.5° each. As a light source, a dual-cavity Nd:YAG laser (made by Dantec, energy: 60mJ per pulse at 532 nm) with modular sheet optics was pulsed twice at a specified time separation. The time-interval was chosen to give maximum pixel displacements to be 8 pixels, as shown in Table 2.1. Images were taken when synchronized pulses from a pulse generator (made by IDT, eight channels, resolution: 20 ns) double-triggered the cameras and laser. The imaging trigger was repeated ten times a second to have enough time gap longer than turbulent time scales so that stochastic independence of the samples can be maintained. Alumina particles with a nominal size of $0.3 \mu\text{m}$ were used as flow

tracers. As compressed air was pumped into a seeder, the fluidized particles moved to a cyclone separator which removed the large particle agglomerates. Subsequently, the fine alumina particles were sprayed as tracers into the chamber through a flexible pipe (inner dia. 8 mm, outer dia. 12 mm).

The SPIV interrogation was performed using Insight 4G 11.1 software (made by TSI, stereo processing). At first, a stereo-calibration map was obtained using images of a calibration target, with cubic polynomial regression for in-plane directions and linear regression for the out-of-plane direction. The mapping procedure was based on the back-projection of three-dimensional geometry and the elimination of image distortions (Soloff *et al.*, 1997). All images were dewarped according to the 3D-calibration map using the cardinal spline interpolation method. Two-dimensional PIV interrogation utilized FFT correlator as the cross-correlation engine with the window deformation method. The first interrogation window size was 64px with 50% overlap, and the second one was 32px with the same overlap ratio. The local median test was then applied to detect outliers, which is appropriate for a homogeneous flow field (Westerweel, 1994; Westerweel & Scarano, 2005), and either local median or valid secondary peak replaced the bad vectors. Finally, the vector fields of full three-components were reconstructed according to the calibration map. Some major PIV interrogation parameters are shown in Table 2.2.

Table 2.1 Experimental conditions

Case	Woofer amplification [dB]	Time-interval Δt [μ s]	Image pairs N [pair]
1	28	40	2,000
2	26	50	2,000
3	24	60	2,000
4	22	70	2,000
5	20	80	2,000

Table 2.2 PIV interrogation conditions

Window Size [px ²]	32×32
Overlap Ratio [%]	50
Number of Vectors	101×101
Vector Spacing Δx [mm]	0.368

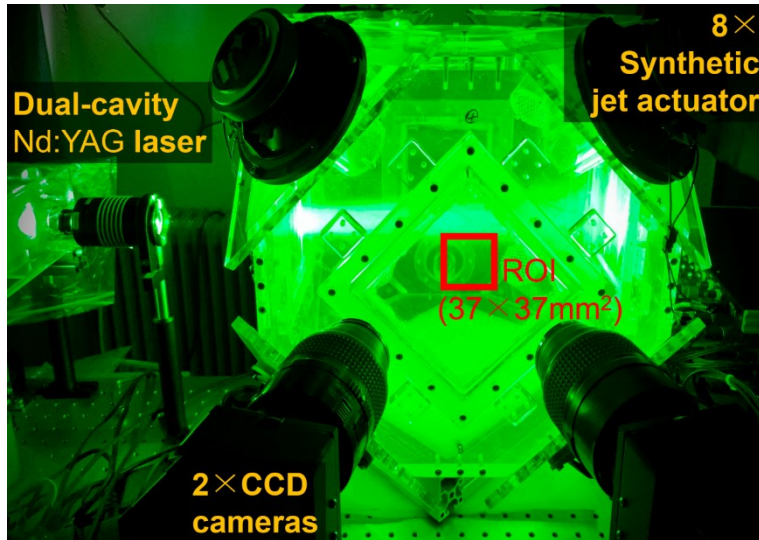


Figure 2.1 Stereo-PIV measurement of HIT chamber

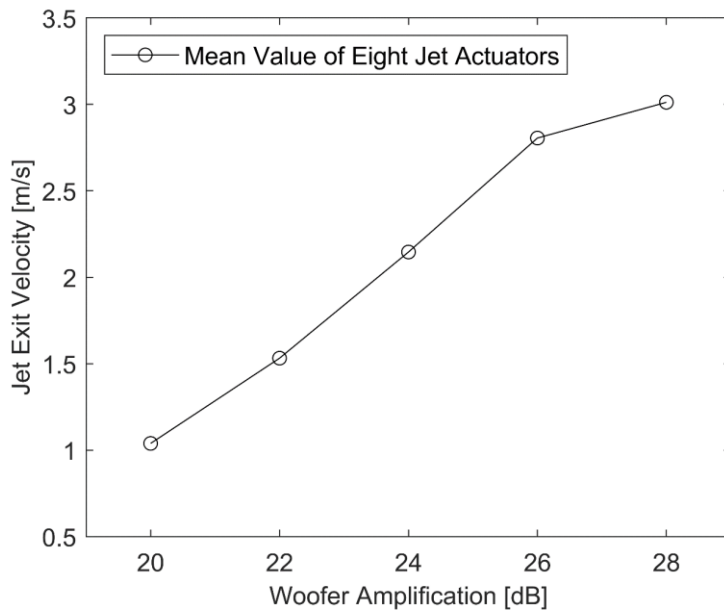


Figure 2.2 Mean jet exit velocity according to the amplifier intensity for the subwoofer speakers

Chapter 3. One-Point Statistics and Flow Quality

3.1. Statistically stationary turbulence

The synthetic jet actuators were constantly activated to attain a set of two thousand independent samples of statistically stationary turbulence for each case. In statistical fluid mechanics, it is generally implied that turbulent flow fields are random in the sense of probability theory. Thus, every single measurement of the flow field can be regarded as “a sample taken from the statistical ensemble of all possible fields” (Monin & Yaglom, 1971). The averaging of the measured flow fields can be understood then as probability averaging concerning the corresponding statistical ensemble. A schematic of two thousand samples from a statistical ensemble is shown in Figure 3.1. To investigate one-point statistics of the experimental results, we assumed time-invariance of turbulence, and obtained a field of ensemble statistics by temporal-averaging. Furthermore, we confirmed the homogeneity, space-invariance of turbulence, and then obtained single ensemble statistics by spatiotemporal-averaging, representing the whole measurement for each case.

A sample velocity field of $Re_\lambda = 228$ is shown in Figure 3.2(a). The vector map depicts x- and y-directional velocities, while the color map quantifies the out-of-plane velocities. The mean velocity field that is ensemble-averaged over two thousand samples for the same case is shown in Figure 3.2(b). Note that the reference scale is expanded by three-times. The mean flow, compared to the instantaneous flow, has a small velocity magnitude with little spatial variation, which means nearly zero mean-flow and zero mean-strain.

3.2. Evaluation of flow quality

The fluctuating component of velocity $u_i'(x_1, x_2)$ ($i = 1,2,3$), was obtained by subtracting the local mean velocity $U_i(x_1, x_2)$ from the measured instantaneous velocity $u_{i,meas}(x_1, x_2)$. Hereinafter, the fluctuating component will be denoted by $u_i(x_1, x_2)$ for brevity. We obtained the probability density functions (PDFs) of the velocity fluctuation from the whole spatial field and time duration for each case, normalized by the local root-mean-square (RMS) velocity $u_{i,RMS}(x_1, x_2)$, as shown in Figure 3.3. The u_1 (horizontal), u_2 (vertical), and u_3 (out-of-plane) velocity components closely follow the standard Gaussian profile, with skewness $S \approx 0$ and kurtosis $K \approx 3$ as shown in Table 3.1, which implies the turbulence is stationary (Mouri *et al.*, 2002).

The homogeneity was evaluated by examining the spatial distribution of the turbulent kinetic energy (TKE; k)

$$k(x_1, x_2) = \frac{1}{2} u_{i,RMS}(x_1, x_2) u_{i,RMS}(x_1, x_2) \quad (i=1,2,3) \quad (\text{Eq.3.1})$$

normalized by the spatial-average of TKE $\langle k \rangle$, as shown in Figure 3.4(a). The distribution is uniform with little variation in space, which means the turbulence is homogeneous compared to previous literature (Goepfert *et al.*, 2010; Chang *et al.*, 2012). Figure 3.4(b) shows the range that contains ninety-five percent of values, and verifies good homogeneity for the other conditions as well.

The isotropy was similarly evaluated by examining the spatial distribution of the ratio between RMS velocity quantities $u_{j,RMS}(x_1, x_2) / u_{i,RMS}(x_1, x_2)$, which also has uniform spatial distribution as shown in Figure 3.5(a). Figure 3.5(b) shows the mean and the range containing ninety-five percent of values of the RMS velocity ratio, which verifies good isotropy for the other conditions as well. Here, the mean value

of $u_{2,\text{RMS}}/u_{1,\text{RMS}}$ and $u_{3,\text{RMS}}/u_{2,\text{RMS}}$ are biased from unity because the intensity of velocity fluctuation in the vertical direction $u_{2,\text{RMS}}$ is slightly smaller than that in the other directions.

Furthermore, spatial velocity derivatives $\partial_i u_j$ were calculated by central differencing of the velocity fluctuation fields, and then the PDFs of velocity derivatives were drawn as shown in Figure 3.6. Their statistical moments are summarized in Table 3.2. First, we found that longitudinal derivatives are negatively skewed, while transverse derivatives are not skewed. The skewness S values of longitudinal derivatives were -0.346 and -0.395, which agree with previous work (Vincent & Meneguzzi, 1991; Sreenivasan & Antonia, 1997; Bos *et al.*, 2012). The negative skewness S is a direct consequence of the nonlinearity of the Navier-Stokes equation, representing the production rate of mean-square vorticity by vortex stretching (Tavoularis *et al.*, 1978). Moreover, both directional derivatives showed highly intermittent characteristics with the kurtosis K up to 6.28. These phenomena were also reported in the literature (Sreenivasan & Antonia, 1997; Gotoh *et al.*, 2002; Bos *et al.*, 2012), which reported the intermittency of energy dissipation and high-strain (Ishihara *et al.*, 2009; Davidson, 2015).

To have a wide range of turbulence conditions, we controlled the amplifier intensity of the subwoofer speakers that are mounted on the synthetic jet actuators. We confirmed that the TKE varies according to the change of woofer amplification, as shown in Figure 3.7(a). The TKE values were plotted according to the jet exit velocities measured in Figure 2.2, which shows a linear correlation. Here, TKE-3C is calculated from the full three velocity components, while TKE-2C is from two in-plane components, as a reference. The variation of TKE values in the figure implies the ability to generate turbulence under various conditions with our experimental setup.

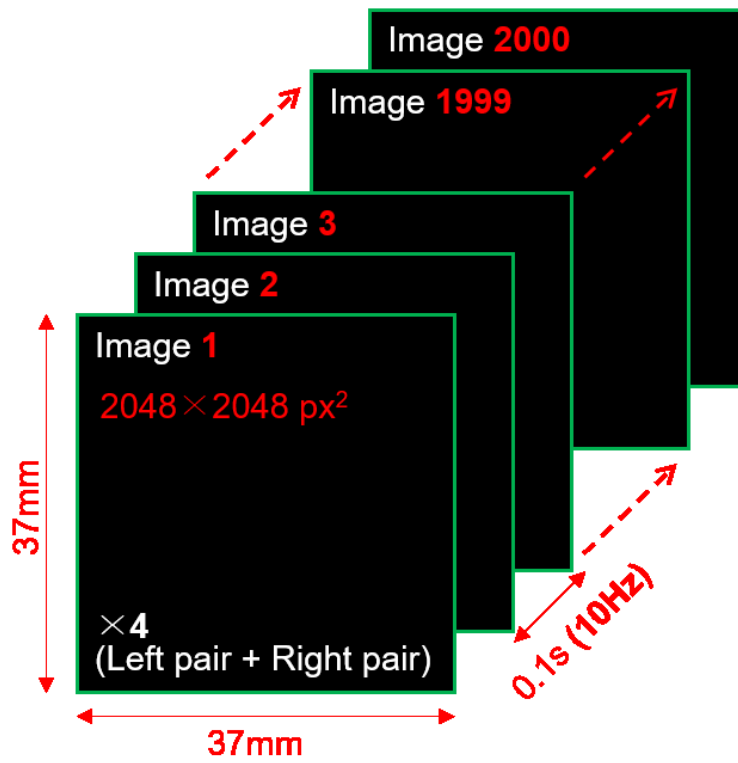


Figure 3.1 Independent samples taken from a statistical ensemble

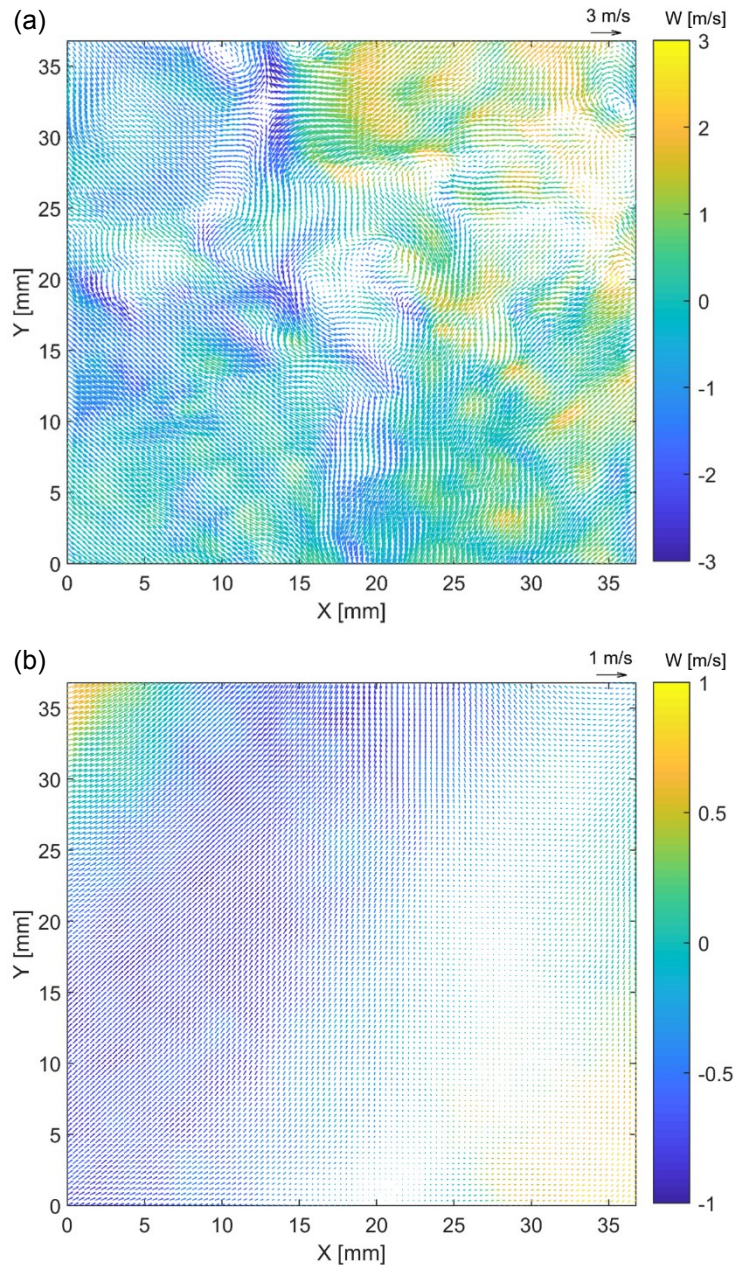


Figure 3.2 Example flow field (case 1): vector map for in-plane velocity and color map for out-of-plane velocity (a) Instantaneous velocity field (b) Mean velocity field from 2,000 samples; Note that the reference scale is expanded by three-times

Table 3.1 Statistical moments of velocity fluctuations (case 1)

	Velocity RMS (2 nd)	S (3 rd)	K (4 th)
u_1	1.056 m/s	+0.035	2.99
u_2	0.985 m/s	+0.078	3.19
u_3	1.058 m/s	-0.088	3.44
Gaussian	-	0	3.00

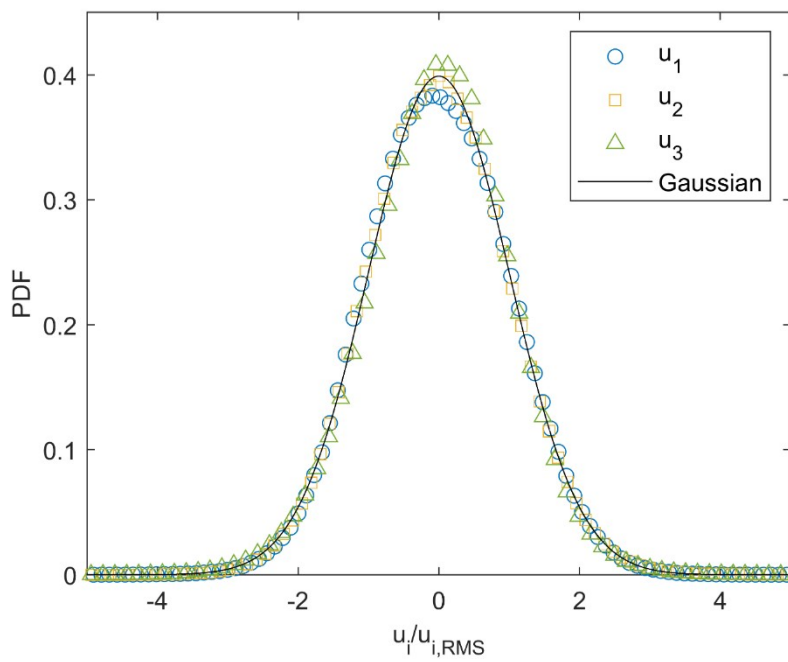


Figure 3.3 Probability density functions of velocity fluctuations (case 1)

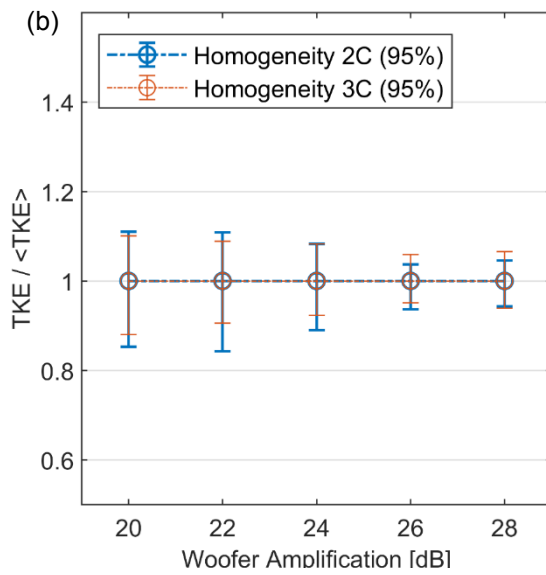
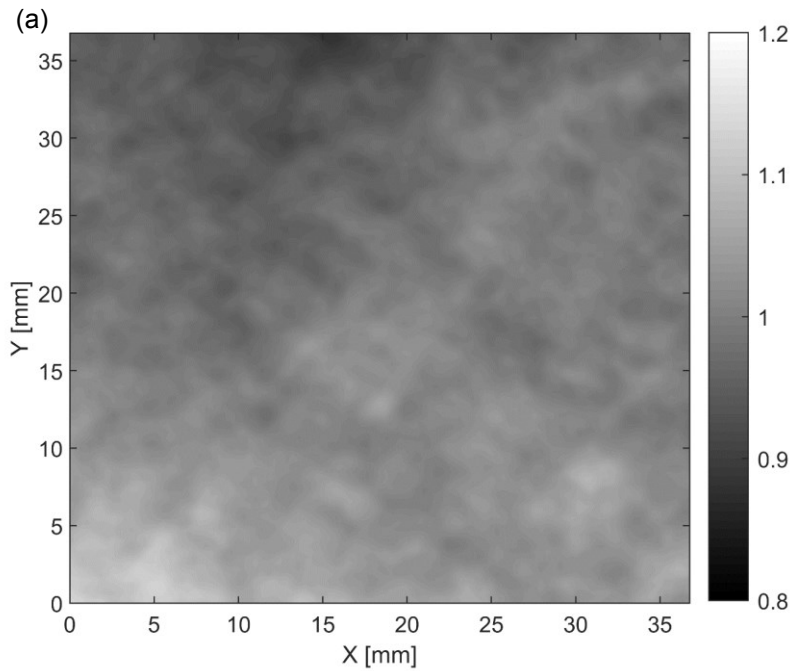


Figure 3.4 Homogeneity plot (a) Map of $\frac{k(x_1, x_2)}{\langle k \rangle}$ (case 1): 95% values in 0.939-1.066 (b) Homogeneity quantities in other conditions; the intervals show the range that contains 95% values

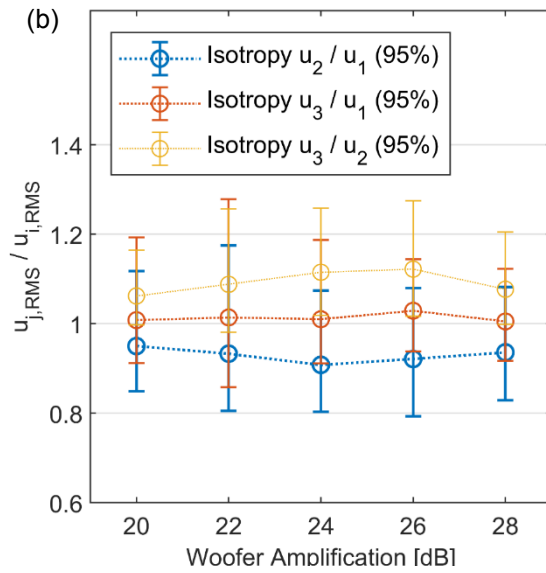
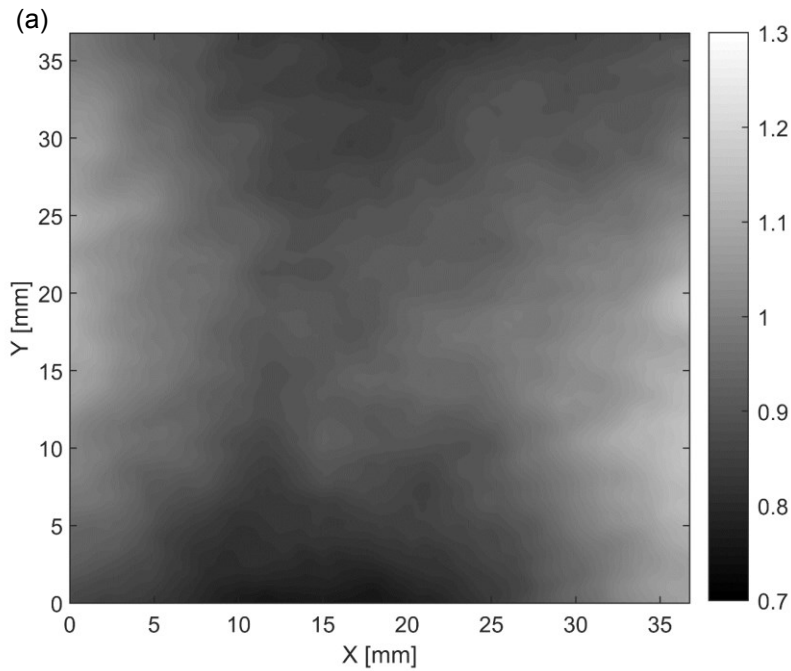


Figure 3.5 Isotropy plot (a) Map of $\frac{u_{2,RMS}(x_1, x_2)}{u_{1,RMS}(x_1, x_2)}$ (case 1): 95% values in 0.829-1.082 (b) Isotropy quantities in other conditions and in other directions; the intervals show the range that contains 95% values

Table 3.2 Statistical moments of velocity derivatives (case 1)

		S (3 rd)	K (4 th)
Longitudinal	$\partial_1 u_1$	-0.346	4.81
	$\partial_2 u_2$	-0.395	5.07
Transverse	$\partial_2 u_1$	+0.015	6.23
	$\partial_2 u_3$	+0.001	6.28
Gaussian		0	3.00

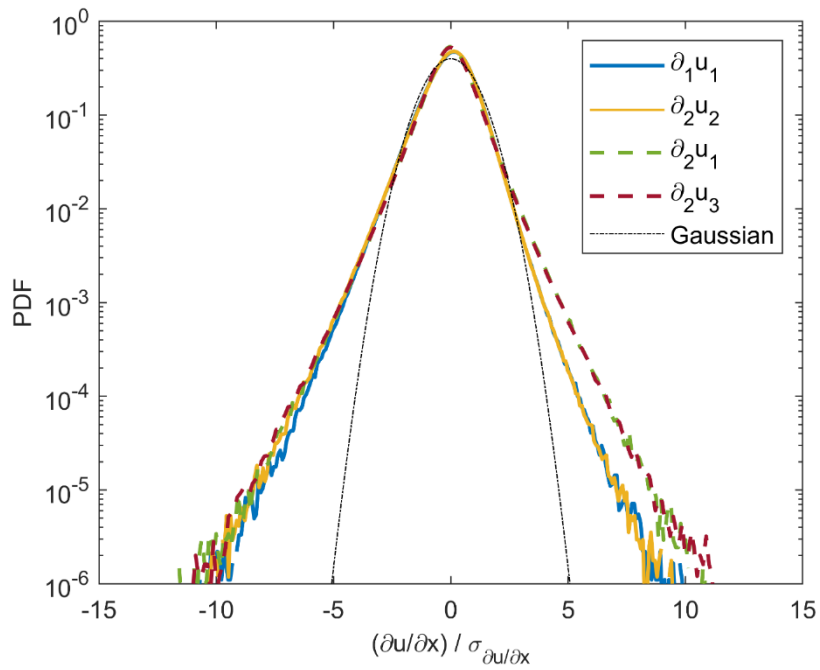


Figure 3.6 Probability density functions of velocity derivatives (case 1): longitudinal derivatives in solid lines and transverse derivatives in dashed lines

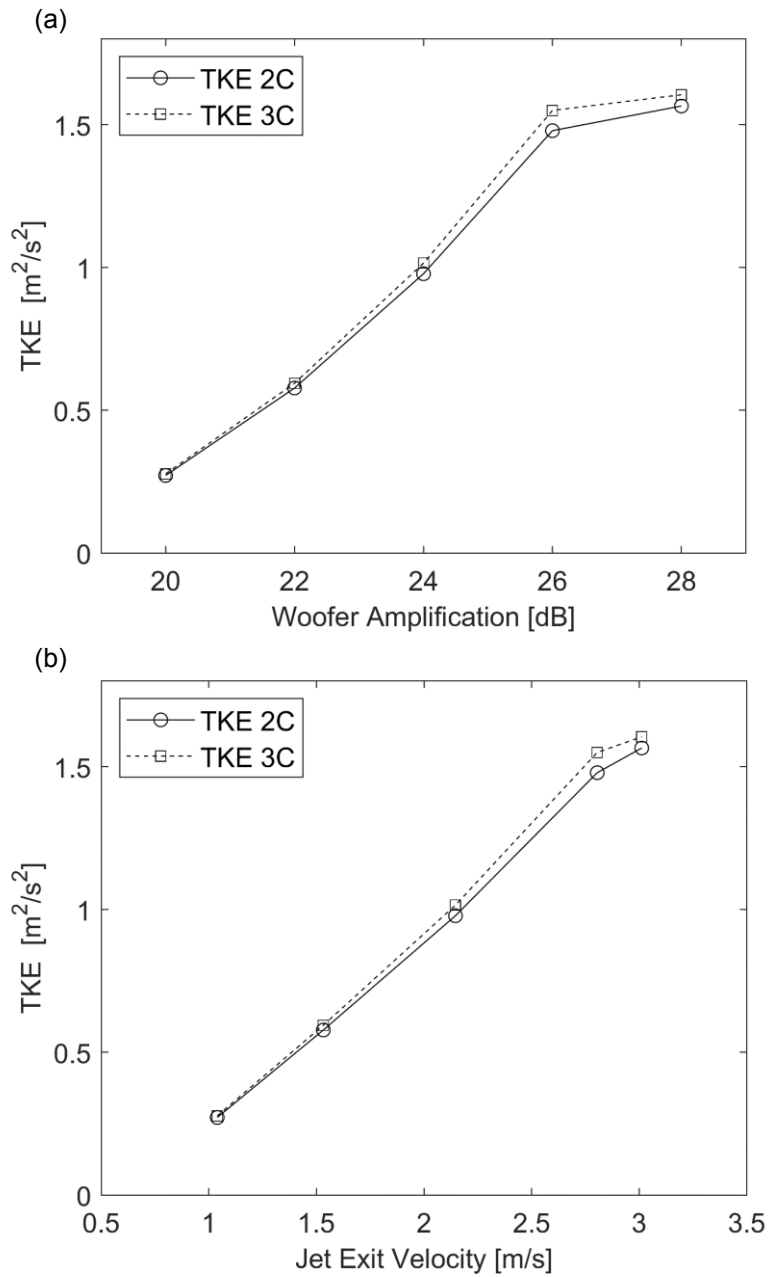


Figure 3.7 Turbulent kinetic energy (TKE) for each case (a) TKE varying with the woofer amplification level (b) TKE variation with the jet exit velocity, showing a more linear correlation

Chapter 4. Two-Point Statistics and Flow Scale

4.1. Velocity correlation function

Two-point spatial velocity correlation functions were calculated. The longitudinal velocity correlation functions are defined as follows, where $F_{uu}(r)$ denotes the longitudinal correlation of the horizontal velocities and $F_{vv}(r)$ denotes the vertical one.

$$F_{uu}(r) = \langle u_1(x_1, x_2)u_1(x_1 + r, x_2) \rangle / \langle u_{1,\text{RMS}}^2 \rangle \quad (\text{Eq.4.1})$$

$$F_{vv}(r) = \langle u_2(x_1, x_2)u_2(x_1, x_2 + r) \rangle / \langle u_{2,\text{RMS}}^2 \rangle \quad (\text{Eq.4.2})$$

The transverse velocity correlation functions are defined as follows, where $G_{uu}(r)$ denotes the transverse correlation of the horizontal velocities.

$$G_{uu}(r) = \langle u_1(x_1, x_2)u_1(x_1, x_2 + r) \rangle / \langle u_{1,\text{RMS}}^2 \rangle \quad (\text{Eq.4.3})$$

Figure 4.1(a) shows the longitudinal velocity correlation functions $F(r)$ in two different directions: solid lines for horizontal and dashed lines for vertical. The point is that each pair of solid and dashed lines are in a nearly exact agreement over the whole range of r , which demonstrates the scale-to-scale isotropy of the turbulence. Moreover, Figure 4.1(b) shows the transverse correlation $G(r)$, and the $G_{\text{iso}}(r)$ that is from the isotropy relation (Eq.4.4). We find that each pair of solid and dashed lines are also in agreement, which means the isotropy relation in HIT theory (von Karman & Howarth, 1937) holds in the measured turbulence, verifying the scale-to-scale isotropy of the turbulence.

$$G(r) \approx G_{\text{Iso}}(r) = F(r) + \frac{r}{2} \frac{\partial F(r)}{\partial r} \quad (\text{Eq.4.4})$$

The integral length scale (L_{ii}) was estimated by integrating the extrapolated longitudinal velocity correlation function, as follows.

$$L_{ii} = \int_0^{\infty} F_{ii}(r) dr \quad (\text{Eq.4.5})$$

The extrapolation of $F(r)$ is inevitable because we cannot measure the tail of $F(r)$ for which r is greater than 37mm, within the experimental setup. The exponential extrapolation procedure is illustrated in Figure 4.2(a); we made a linear regression model in the logarithmic space so that we obtain an exponential regression model in the linear space. Here, we only used the samples in the middle of the curve in order to exclude relatively unreliable samples at both ends. The full longitudinal velocity correlation function including the extrapolated data is shown in Figure 4.2(b). The estimated integral length scales and their ratios are summarized in Table 4.1, where the ratio is close to unity, demonstrating large-scale isotropy (Carter & Coletti, 2017). Moreover, the values seem to be independent of the turbulence conditions for cases 1 to 5. This result implies the large-scale similarity of turbulence in the five different conditions, likely due to the fixed chamber size.

4.2. Second-order structure-function

The second-order structure functions were calculated. We hereinafter refer to the second-order structure function as structure-function (SF) for brevity. The longitudinal structure functions are defined as follows, where $D_{LLu}(r)$ denotes the longitudinal structure-function of the horizontal velocities and $D_{LLv}(r)$ denotes the vertical one.

$$D_{LL}u(r) = \langle \{u_1(x_1 + r, x_2) - u_1(x_1, x_2)\}^2 \rangle / 2 \langle u_{1,RMS}^2 \rangle \quad (\text{Eq.4.6})$$

$$D_{LL}v(r) = \langle \{u_2(x_1, x_2 + r) - u_2(x_1, x_2)\}^2 \rangle / 2 \langle u_{2,RMS}^2 \rangle \quad (\text{Eq.4.7})$$

The transverse structure functions are defined as follows, where $D_{TT}u(r)$ denotes the transverse structure-function of the horizontal velocities and $D_{TT}v(r)$ denotes the vertical one.

$$D_{TT}u(r) = \langle \{u_1(x_1, x_2 + r) - u_1(x_1, x_2)\}^2 \rangle / 2 \langle u_{1,RMS}^2 \rangle \quad (\text{Eq.4.8})$$

$$D_{TT}v(r) = \langle \{u_2(x_1 + r, x_2) - u_2(x_1, x_2)\}^2 \rangle / 2 \langle u_{2,RMS}^2 \rangle \quad (\text{Eq.4.9})$$

The longitudinal results are shown in Figure 4.3(a), and the transverse ones are shown in Figure 4.3(b). The main point of Figure 4.3 is that each pair of solid and dashed lines (i.e. horizontal and vertical directions, respectively) are in close agreement over the whole range of r , which reconfirms the scale-to-scale isotropy of turbulence (Carter & Coletti, 2017).

The structure functions display scale information of turbulence, as they have a sharp curvature in the dissipative range, while having a relatively uniform increase in the inertial subrange (IR). In particular, Kolmogorov's second similarity hypothesis states that, when Re_λ is large, the statistical properties of $D(r)$ have a universal form that is uniquely determined by r and the dissipation rate ε alone in the inertial subrange (IR) (Kolmogorov, 1941a, b), validated by elaborate experiments (Saddoughi & Veeravalli, 1994) and high-resolution direct numerical simulations (DNS) (Wang *et al.*, 1996). This statement, after dimensional analysis, leads to the two-thirds law as follows. Here, C_2 is a constant and $4.02C_1 \approx 2.12$, where C_1 is a universal empirical constant of 0.53 (Sreenivasan, 1995; Yeung & Zhou, 1997).

$$D_{LL}(r) = C_2 \varepsilon^{2/3} r^{2/3} \quad (\text{in the IR}) \quad (\text{Eq.4.10})$$

$$D_{TT}(r) = (4/3)C_2 \varepsilon^{2/3} r^{2/3} \quad (\text{in the IR}) \quad (\text{Eq.4.11})$$

4.3. Energy spectrum

The one-dimensional (1D) energy spectra were obtained using fast Fourier-transform (FFT) of velocity fields. To be specific, the spectra of each line for each direction from the velocity fields were first calculated, and then ensemble-averaged over all the image pairs. The results are shown as markers in Figure 4.4(a) and Figure 4.4(b), where the longitudinal spectra are denoted by $E_{\alpha\alpha}(k_\alpha)$ and the transverse spectra are denoted by $E_{\beta\beta}(k_\alpha)$. Furthermore, the longitudinal one-dimensional energy spectra were also calculated in another way, shown as solid lines in Figure 4.4(b), using the cosine-transform of the extrapolated longitudinal velocity correlation functions (Section 4.1), as follows.

$$E_{\alpha\alpha}(k_\alpha) = \frac{2}{\pi} \langle u_{\alpha,RMS}^2 \rangle \int_0^\infty F_{\alpha\alpha}(r) \cos(k_\alpha r) dr \quad (\text{Eq.4.12})$$

In Figure 4.4, the one-dimensional energy spectra in the lower-wavenumber region can be scaled by a -5/3 slope. This is clear evidence that we measure the inertial subrange (Eq.4.13-14), a direct result from Kolmogorov's second similarity hypothesis.

$$E_{\alpha\alpha}(k_\alpha) = C_1 \varepsilon^{2/3} k_\alpha^{-5/3} \quad (\text{in the IR}) \quad (\text{Eq.4.13})$$

$$E_{\beta\beta}(k_\alpha) = (4/3)C_1 \varepsilon^{2/3} k_\alpha^{-5/3} \quad (\text{in the IR}) \quad (\text{Eq.4.14})$$

In the higher-wavenumber region, the spectra using FFT (markers in Figure 4.4(a))

show long tails, which is typical due to noise in the measurement. The spectra using cosine-transform of $F(r)$ (lines in Figure 4.4(a)) show a fluctuating pattern, which is typical of the Fourier-transform result of a gate function corresponding to the PIV interrogation window (Foucaut *et al.*, 2004). In addition, the 1D spectra in the four different directions are in good agreement (Figure 4.4(b)), which supports the scale-to-scale isotropy of turbulence.

The radial two-dimensional (2D) energy spectra were also calculated. The radial 2D spectrum of α -directional velocities is defined by the sum over an annulus radius k in wavenumber space (Liu *et al.*, 1994):

$$E_{\alpha\alpha}(k) = \sum_{k_1^2+k_2^2=k^2} u_{\alpha}(k_1, k_2)u_{\alpha}^*(k_1, k_2). \quad (\text{Eq.4.15})$$

Here, $u_{\alpha}^*(k_1, k_2)$ is the complex conjugate of $u_{\alpha}(k_1, k_2)$, where $u_{\alpha}(k_1, k_2)$ is the result of the two-dimensional Fourier transform of the velocity field $u_{\alpha}(x_1, x_2)$ (Eq.4.16); the value $M=101$ and $N=101$ are the number of vectors in Table 2.2.

$$u_{\alpha}(k_1, k_2) = \sum_{m=1}^M \sum_{n=1}^N u_{\alpha}(x_{1m}, x_{2n})e^{-i(x_{1m}k_1+x_{2n}k_2)} \quad (\text{Eq.4.16})$$

The results are shown in Figure 4.5, where the minus five-thirds law also scales the spectra in the lower-wavenumber region. From Kolmogorov's similarity hypothesis, the radial 2D energy spectra in the inertial subrange follow the formula below (Liu *et al.*, 1994), the constant C_k being 1.64 (Sreenivasan, 1995; Yeung & Zhou, 1997).

$$E_{\alpha\alpha}(k) = 0.535C_k\varepsilon^{2/3}k^{-5/3} \quad (\text{in the IR}) \quad (\text{Eq.4.17})$$

The one- and two-dimensional energy spectra have a peak at the lowest-wavenumber, and decrease in intensity with wavenumber. However, this shape is counterintuitive in that the actual eddy size distribution should be dominant at a finite

length-scale, not at the lowest-wavenumber. The reason of this shape is the “aliasing effect,” where the low-dimensional spectrum misinterprets a wave of wavenumber k as being one of wavenumber $k \cos\theta$, θ for the degree between the wave and its orthogonal projection onto the low-dimensional space, resulting in the energy of the wave appearing closer to the origin in spectral space (Davidson, 2015). Therefore, the low-dimensional energy spectra do not represent the actual energy density distribution of turbulent eddies (waves) in physical space. On the other hand, the full three-dimensional energy spectrum, which is unobtainable using the stereoscopic measurement in a planar domain, can distinguish, but still not precisely quantify, the actual distribution of eddies in turbulence.

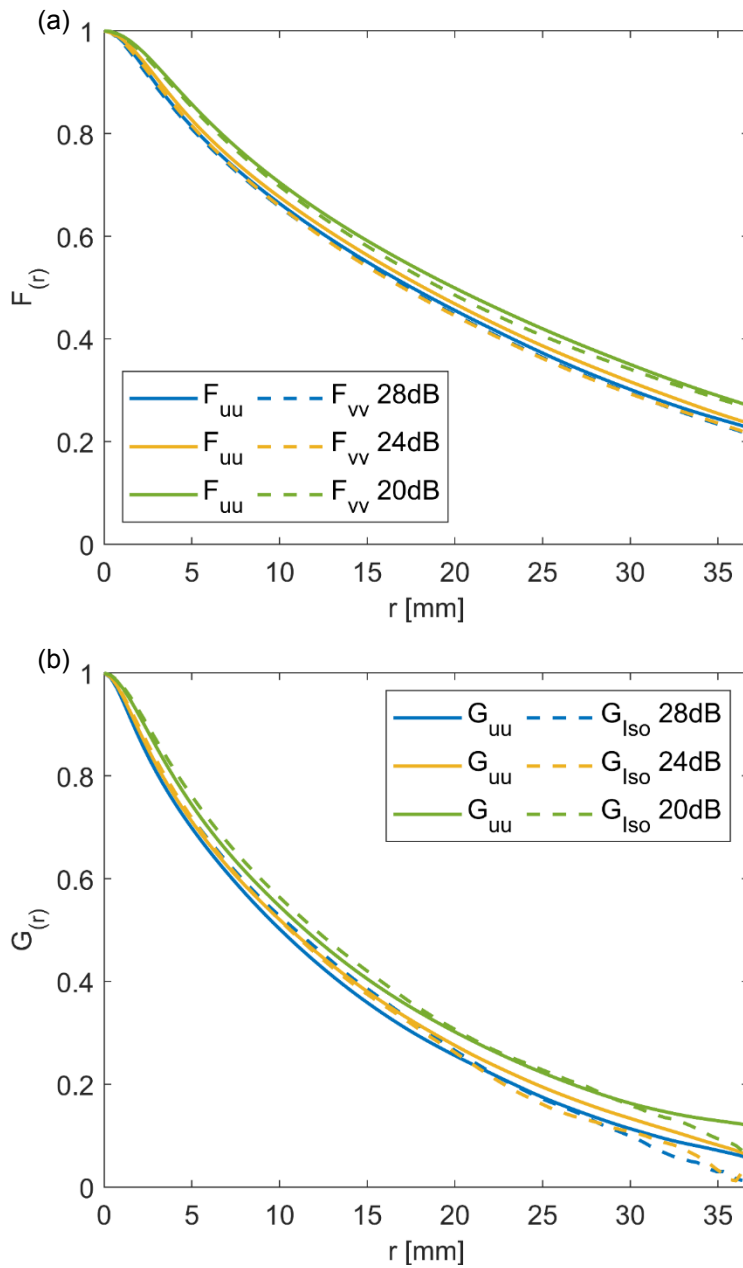


Figure 4.1 Velocity correlation functions (case 1, 3, 5) (a) Longitudinal velocity correlation functions (b) Transverse velocity correlation functions plotted against the isotropy relation

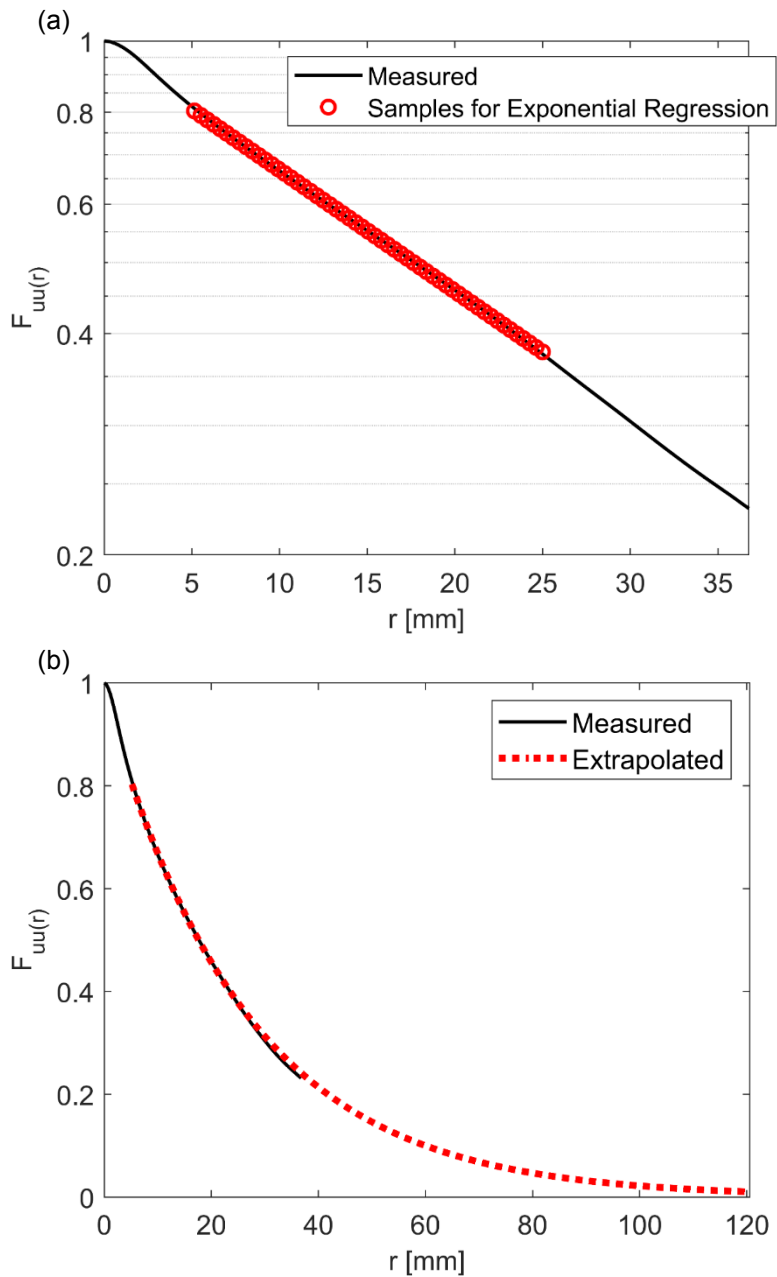


Figure 4.2 Procedure to obtain the extrapolated longitudinal velocity correlation function (case 1, horizontal velocities) (a) Exponential regression in the logarithmic graph (b) Full velocity correlation function including the extrapolated data

Table 4.1 Estimated integral length scales and ratios

Case	L_{11} (horizontal) [mm]	L_{22} (vertical) [mm]	L_{11} / L_{22}
1	28.99	27.14	1.068
2	28.92	27.83	1.039
3	26.98	24.14	1.118
4	26.21	25.42	1.031
5	25.70	24.69	1.041

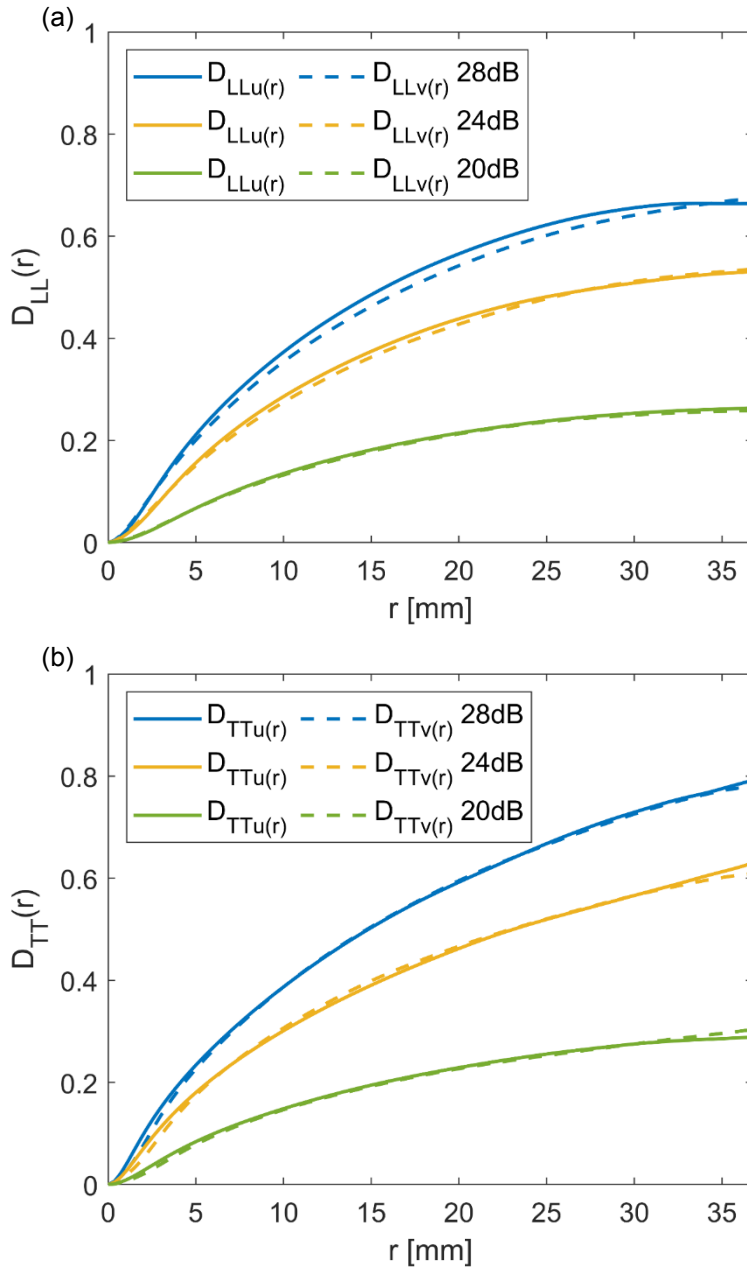


Figure 4.3 Second-order structure functions (case 1, 3, 5) for two different directions (a) Longitudinal structure functions (b) Transverse structure functions

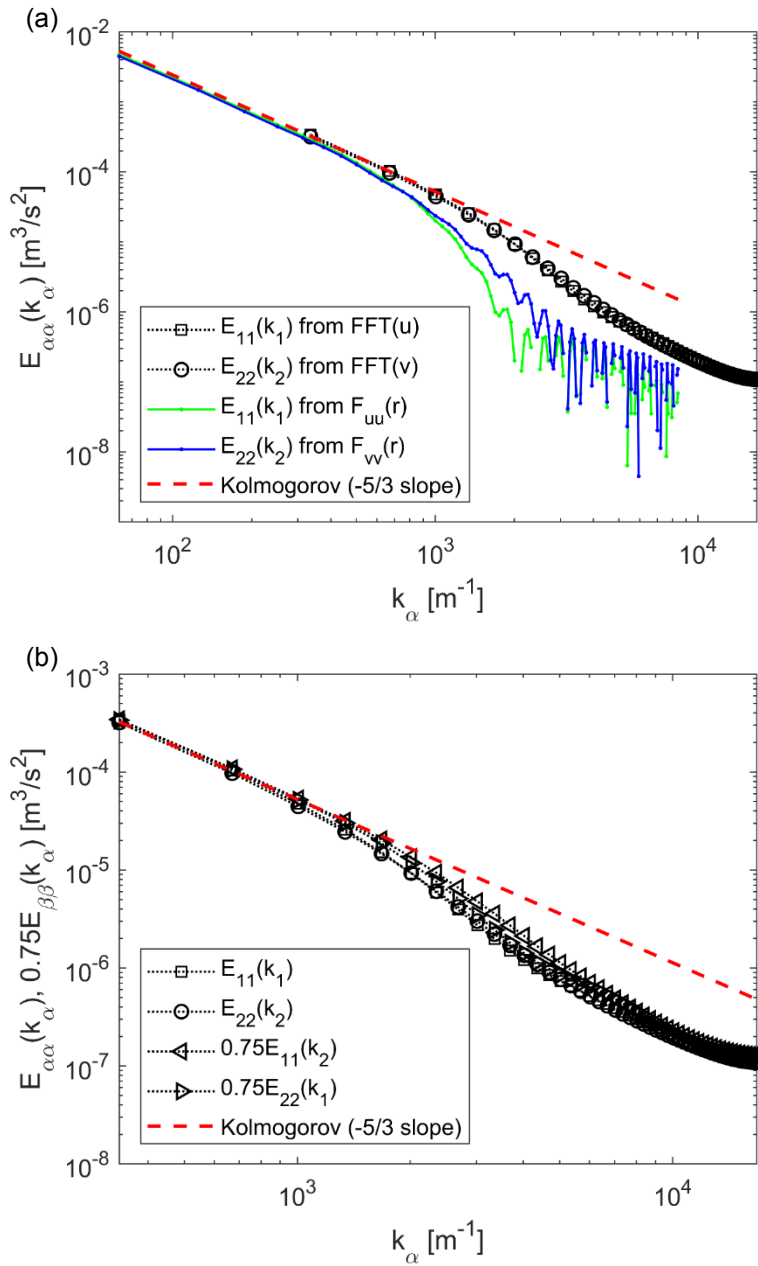


Figure 4.4 One-dimensional energy spectra (case 1) (a) Longitudinal 1D energy spectra using two different methods (b) Longitudinal and transverse 1D energy spectra

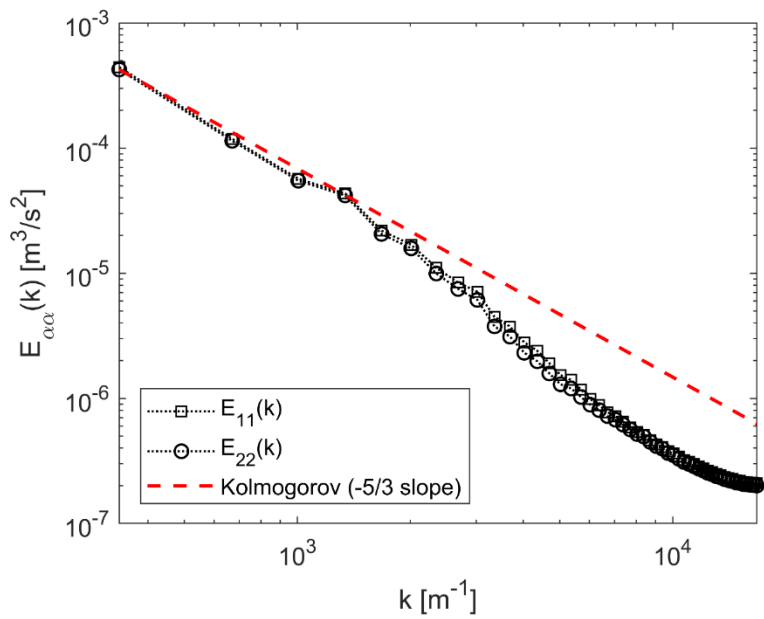


Figure 4.5 Radial two-dimensional energy spectra (case 1)

Chapter 5. Measurement of Dissipation Rate

5.1. Direct method

The dissipation rate ε is the rate of the dissipation of mechanical energy per unit mass in a viscous fluid, which is calculated by the working rate of viscous stress per unit mass, as follows.

$$\varepsilon = \frac{1}{\rho} \tau_{ij} S_{ij} \quad (\text{Eq.5.1})$$

The viscous stress τ_{ij} for a Newtonian fluid is defined as Eq.5.2, since the viscous stress and the strain rate $S_{ij} = \frac{1}{2} \left(\frac{\partial u_i}{\partial x_j} + \frac{\partial u_j}{\partial x_i} \right)$ have a linear correlation with the coefficient being twice the dynamic viscosity $\mu (= \rho\nu)$.

$$\tau_{ij} = 2\mu S_{ij} \quad (\text{Eq.5.2})$$

Consequently, the dissipation rate ε in a Newtonian fluid can be directly calculated from the following formula: the substitution of Eq.5.2 into Eq.5.1.

$$\varepsilon = 2\nu S_{ij} S_{ij} = \nu \frac{\partial u_i}{\partial x_j} \left(\frac{\partial u_i}{\partial x_j} + \frac{\partial u_j}{\partial x_i} \right) \quad (\text{Eq.5.3})$$

The PIV measurement of a planar domain cannot return full-components of strain rate tensor S_{ij} because the PIV does not measure the velocity gradient in the out-of-plane direction. Some researchers have tried to utilize two SPIV systems simultaneously to obtain the full strain rate tensor (Foucaut *et al.*, 2016), whereas the measurement domain should be reduced to a line, thus impractical for three-dimensional flows. Instead, we adopt the continuity equations (Eq.5.4) and the

isotropy relations (Eq.5.5) to estimate the full strain rate tensor in a quadratic form (Eq.5.6) (Doron *et al.*, 2001).

$$\left(\frac{\partial u_3}{\partial x_3}\right)^2 = \left(\frac{\partial u_1}{\partial x_1} + \frac{\partial u_2}{\partial x_2}\right)^2 \quad (\text{Eq.5.4})$$

$$\left. \begin{aligned} \left(\frac{\partial u_i}{\partial x_j}\right)^2 &\approx \left(\frac{\partial u_k}{\partial x_l}\right)^2 \\ \frac{\partial u_i}{\partial x_j} \frac{\partial u_j}{\partial x_i} &\approx \frac{\partial u_k}{\partial x_l} \frac{\partial u_l}{\partial x_k} \end{aligned} \right\} (i \neq j \ \& \ k \neq l) \quad (\text{Eq.5.5})$$

$$S_{ij}S_{ij} = 2\left(\frac{\partial u_1}{\partial x_1}\right)^2 + 2\left(\frac{\partial u_2}{\partial x_2}\right)^2 + 2\left(\frac{\partial u_1}{\partial x_1} \frac{\partial u_2}{\partial x_2}\right) + \frac{3}{2}\left(\frac{\partial u_1}{\partial x_2} + \frac{\partial u_2}{\partial x_1}\right)^2 \quad (\text{Eq.5.6})$$

Moreover, we apply a correction to Eq.5.3 to eliminate the dominant random error term of PIV measurements when directly calculating the dissipation rate ε (Eq.5.7) (Tanaka & Eaton, 2007); $\varepsilon|_{\Delta x}$ denotes the dissipation rate of Eq.5.3 using the velocity derivatives from the central differencing with Δx grid spacing, while $\varepsilon|_{2\Delta x}$ denotes that with $2\Delta x$ grid spacing.

$$\varepsilon_{direct}(x_1, x_2) = \frac{1}{3} [4\varepsilon|_{2\Delta x}(x_1, x_2) - \varepsilon|_{\Delta x}(x_1, x_2)] \quad (\text{Eq.5.7})$$

In general, however, this direct method of dissipation rate calculation is inapplicable to PIV measurements of turbulence, because the limited spatial resolution of the PIV interrogation windows cannot capture the smallest fluid motions that are necessary to obtain the actual strain rate. Therefore, unless we employ a super-resolution PIV method that can resolve the Kolmogorov length-scale η , we can utilize the following four methods that are based on the universal scaling law of HIT (Section 5.2 – 5.3), large-scale energy budget (Section 5.4), or large-eddy simulation (LES) analogy (Section 5.5).

5.2. Structure-function fitting method

The first method to accurately measure the dissipation rate ε is the structure-function (SF) fitting method that is based on Kolmogorov's second similarity hypothesis in the inertial subrange (IR), formulated in Eq.4.10-11. In the equations, the structure-function $D(r)$ is a directly obtainable value as a function of r , and the constant C_2 is a universal constant of 2.12. Thus, as we reverse the formulae, we can estimate the dissipation rate in the inertial subrange (de Jong *et al.*, 2009) as follows.

$$\varepsilon = (1/r)[D_{LL}(r)/C_2]^{3/2} \quad (\text{in the IR}) \quad (\text{Eq.5.8})$$

$$\varepsilon = (1/r)[D_{TT}(r)/(4C_2/3)]^{3/2} \quad (\text{in the IR}) \quad (\text{Eq.5.9})$$

The dissipation rate measurements using the compensated longitudinal SF (Eq.5.8) are shown in Figure 5.1(a), and the measurements using the compensated transverse SF (Eq.5.9) are shown in Figure 5.1(b). Both compensated SFs show plateaus, which imply the inertial subrange. We take the maximum point of the slightly convex curve in each plateau region as the estimated dissipation rate ε value, shown as dashed lines in the figure. The quantities are summarized in Figure 5.2(a). The circle markers correspond to Figure 5.1(a), while the diamond markers correspond to Figure 5.1(b). We can find that the dissipation rate measurements from the four different SFs are in a good agreement; thus, hereinafter, we use the averaged values over the four quantities for each condition as the results of the structure-function fitting method. Here, the x -axes of the graphs are set to be the jet exit velocities, which are shown in Figure 2.2 and Figure 3.7(b), so the five points correspond to case 1 to 5: woofer amplification 20dB to 28dB.

5.3. Energy spectrum fitting method

The second method is the energy spectrum fitting method that is based on Kolmogorov's second similarity hypothesis in spectral space, formulated in Eq.4.13-14. In these equations, the energy-spectrum $E_{ii}(k_j)$ is a directly obtainable value as a function of wavenumber k_j , and the constant C_1 is a universal constant of 0.53. Therefore, by reversing the formulae in the same way as the previous section (Eq.5.8-9), we can estimate the dissipation rate in the inertial subrange, as follows.

$$\varepsilon = [E_{\alpha\alpha}(k_\alpha)/C_1]^{3/2} k_\alpha^{5/2} \quad (\text{in the IR}) \quad (\text{Eq.5.10})$$

$$\varepsilon = [E_{\beta\beta}(k_\alpha)/(4C_1/3)]^{3/2} k_\alpha^{5/2} \quad (\text{in the IR}) \quad (\text{Eq.5.11})$$

The dissipation rate measurements using the energy spectrum methods (Eq.5.10-11) are shown in Figure 5.3; the quantities were calculated by fitting the -5/3 slope (red dashed line in Figure 4.4) to the energy spectra for each case. The results from the four different energy spectra are in good agreement, and they closely agree with the previous result (ε_{SF}), implying the validity of the two methods through crosschecking.

One difference between the two methods, structure-function fitting and energy spectrum fitting, is the Reynolds number dependence. As the original hypothesis (Kolmogorov, 1941a) has noted, the structure-function follows the scaling laws (Eq.4.10-11) in the inertial subrange when the Taylor microscale Reynolds number is large enough to clearly separate large- and small-scales of turbulence (Pearson & Antonia, 2001; Antonia *et al.*, 2017). Therefore, in the case of small Reynolds number, about less than one hundred, the scaling law might not exactly hold, which results in inaccuracy of the structure-function fitting method. On the other hand, the one-dimensional energy spectrum is relatively independent of the Reynolds number

(Djenidi & Antonia, 2012; Antonia *et al.*, 2014). Thus, the energy spectrum fitting method still holds in the case of small Reynolds number, or even when inhomogeneity occurs. To sum up, the energy spectra method can be applied to turbulence with a wider range of Reynolds numbers, compared to the structure-function fitting method, because the spectrum scaling holds relatively irrespective of the Reynolds number.

In addition, the normalized one-dimensional longitudinal energy spectra $E_{\alpha\alpha}(k_\alpha)/(\varepsilon v^5)^{1/4}$ were calculated and plotted as functions of $k_\alpha \eta$ in Figure 5.4. Here, the ε value in the denominator was from the measured result in Figure 5.3, while the Kolmogorov length scale η was calculated from the following definition.

$$\eta = (v^3/\varepsilon)^{1/4} \quad (\text{Eq.5.12})$$

Figure 5.4 depicts that the normalized energy spectra from the five different turbulence conditions are in an exact agreement with the -5/3 slope region, which verifies the similarity of turbulence in the inertial subrange.

5.4. Dissipation scaling method

The viscous dissipation of turbulent kinetic energy occurs at the smallest scale as mentioned in Section 5.1, whereas the TKE itself comes from large-scale forcing, both of which are described in the classical energy cascade model of turbulence. This energy balance over the two different scales implies that the dissipation rate ε can be directly estimated from the large-scale energy transfer rate Π with a constant C_ε (Vassilicos, 2015), as follows.

$$\varepsilon \approx \Pi = C_\varepsilon u_{i,\text{RMS}}^2 / (L_{ii}/u_{i,\text{RMS}}) = C_\varepsilon u_{i,\text{RMS}}^3 / L_{ii} \quad (\text{Eq.5.13})$$

Here, $u_{i,RMS}^2$ represents large-scale energy and $L_{ii}/u_{i,RMS}$ represents large-scale turnover time; thus, their ratio Π means large-scale energy transfer of turbulent kinetic energy. More precisely, Π quantifies the rate of “energy transfer,” which requires measuring the inertial subrange, in which neither production nor dissipation of energy occurs (Lumley, 1992; McComb *et al.*, 2010), agreeing with our experiment as examined in Chapter 4.

The constant C_ϵ in Eq.5.13 is known as a universal constant of 0.5 when Re_λ is greater than 50 (Sreenivasan, 1984; Ishihara *et al.*, 2009), verified by high-resolution DNS (Kaneda *et al.*, 2003). As an exception, the constant is subject to vary in the case of strong mean shear (Pearson *et al.*, 2002), decaying (Sreenivasan, 1998; Bos *et al.*, 2007), or different large-scale flow topology (Mazellier & Vassilicos, 2008; Thormann & Meneveau, 2014), none of which correspond to our study.

The dissipation rate measurements using the dissipation scaling method are shown in Figure 5.5. The measured values from two different directions agree well with each other, in accord with the previous results using the structure-function fitting method. Therefore, by crosschecking, we can conclude that the three methods: structure-function fitting method, energy spectrum fitting method, and dissipation scaling method work accurately in the SPIV measurement of HIT with this experimental setup. Accordingly, the results in Figure 5.2, 5.3, 5.5 can be regarded as the true values of the dissipation rate of turbulence.

5.5. Large-eddy method

Up to now, we have investigated dissipation rate measurement methods that apply only to the simplest type of turbulence: HIT. However, general turbulence, where statistics vary in space and time, requires a different approach. Here, we

consider the large-eddy method, which is a popular and established method to measure the dissipation rate, and we evaluate its performance for various conditions.

The large-eddy method is based on the idea that the PIV measurement of limited spatial resolution is analogous to large-eddy simulations (LES), in that both of them function as a low-pass filter (Germano, 1992). Because the PIV measurement resolution is in between the large-eddy and sub-grid scales (SGS) as shown in Figure 5.6, the dissipation rate is estimated as the energy transfer at the cutoff wavenumber (Sheng *et al.*, 2000). To be specific, we adopt an eddy viscosity model, namely the Smagorinsky model (Smagorinsky, 1963; Lilly, K., 1966), which is commonly used in LES for SGS stress modelling. The formulation of the large-eddy method is in the following equations (Eq.5.14-15), with the Smagorinsky constant of $C_s = 0.17$. Here, the filter size Δ in LES is replaced by the PIV interrogation window size Δ_{IW} and the strain rate invariant $|S|$ is defined as $(2S_{ij}S_{ij})^{1/2}$ (Meneveau & Katz, 2000).

$$\tau_{ij} = -C_s^2 \Delta^2 |S| S_{ij} \quad (\text{Smagorinsky model}) \quad (\text{Eq.5.14})$$

$$\varepsilon \approx \langle \varepsilon_{SGS} \rangle = -2 \langle \tau_{ij} S_{ij} \rangle = 2^{3/2} C_s^2 \Delta_{IW}^2 \langle S_{ij} S_{ij} \rangle^{3/2} \quad (\text{Eq.5.15})$$

There is an issue regarding the non-universality of the Smagorinsky constant C_s for various turbulence types. The constant value of 0.17 is appropriate for HIT, while it should be adjusted for other kinds of turbulence, such as high-shear flow in a turbulent boundary layer (Deardorff, 1971; Canuto & Cheng, 1997). In LES, to overcome this deficiency, dynamic SGS stress models have been applied, which are based on the idea of calculating the local Smagorinsky constant using two cutoff filters at different sizes (Germano *et al.*, 1991; Lilly, D. K., 1992). Although the Smagorinsky model improved with the dynamic procedure, it is still dependent on the cutoff scale and local flow scale (Meneveau & Lund, 1997). The variability of

the Smagorinsky constant and its scale-dependency imply that the PIV interrogation window size, corresponding to the filter size in LES, can influence the results from the large-eddy method in PIV measurements. This implication has been supported by a PIV experiment (Bertens *et al.*, 2015), and a PIV simulation with a DNS dataset (Lee & Hwang, 2019).

The dissipation rate measurements using the large-eddy method are shown in Figure 5.7. Here, 1C, 2C, 3C denotes the number of velocity components used in the strain rate calculation (Eq.5.4-5), based on the isotropy assumption. The results show that, in comparison with the accurate measurement using SF fitting, the large-eddy method underestimates the dissipation rate when the turbulence intensity is low. This means the large-eddy method underestimates when the normalized PIV resolution is high (Δ_{IW}/η is small): IW size over the smallest Kolmogorov length-scale becomes finer when the turbulence intensity decreases, as shown in the inner box of Figure 5.7.

Underestimation of the dissipation rate with the large-eddy method at high PIV resolution is because the cutoff wavenumber corresponding to the IW size moves to the higher wavenumber region with higher normalized PIV resolution. As a result, the cutoff wavenumber moves to the dissipative region in the spectrum, beyond the inertial subrange. Thus, the large-eddy method, which is based on the SGS flux in the inertial subrange, becomes inapplicable. Therefore, the large-eddy method requires the PIV spatial vector spacing to be in the inertial subrange, which becomes a necessary condition for PIV experimental settings when using this method for dissipation rate calculation.

Nonetheless, the large-eddy method has a great advantage in that it can obtain the dissipation rate at each instant and location with high temporal- and spatial resolution, thus providing the spatiotemporal distribution of the dissipation rate. For

this reason, the large-eddy method can be applied to more general measurements of inhomogeneous or unsteady turbulent flow. PDFs of the dissipation rate, calculated from the large-eddy method, are shown in Figure 5.8. They follow a lognormal distribution. This result verifies Kolmogorov's third similarity hypothesis, which suggests that the dissipation rate shows an asymptotic behavior of lognormal dispersion in homogeneous turbulence (Kolmogorov, 1962; Kraichnan, 1974). Moreover, the profile becomes closer to a lognormal distribution when a larger number of velocity components are used in calculating the strain rate, indicating the necessity of 3D measurements to investigate the distribution of viscous dissipation.

5.6. Comparison

Five different methods for dissipation rate measurement have been investigated, including the direct method. Figure 5.9 compares these five results in a single plot. The first three lines show the three accurate measurements from Section 5.2-4, two of which utilize the universal scaling laws in the inertial subrange: structure-function fitting and energy spectrum fitting methods, and the other utilizes energy scaling between energy-production and dissipation scales: dissipation scaling method. Next, the large-eddy method shows underestimation with smaller turbulence intensity due to the excessive PIV resolution compared to the smallest turbulence length-scale, as outlined in Section 5.5. Finally, the results of the direct method are depicted in this figure as triangular markers. The direct method underestimates the dissipation rate for all five conditions, because the PIV resolution is larger than the Kolmogorov length-scale, and thus the smallest fluid motions cannot be resolved. We observe that the discrepancy becomes larger with coarser normalized PIV resolution, as the insufficiency of the spatial resolution becomes worse.

The repeatability of each method has been checked to examine the reliability of each measurement method. Figure 5.10 shows the results, in which we divided two thousand samples into ten sets of two hundred samples each, and plot the calculation result of each set in the figure. The order of the five methods on the x -axis is according to the magnitude of the mean value. We find that the dissipation scaling method has the widest confidence interval (CI) indicating the largest random error, whereas the direct method has the narrowest CI indicating the least random error. The other three methods: large-eddy method, structure-function fitting method, and energy spectrum fitting method, show a similar extent of CI, indicating a similar random error. The dissipation scaling method has highest uncertainty, because it is influenced by the direct propagation of uncertainty in the integral length scale L_{ii} as shown in Eq. 4.5.

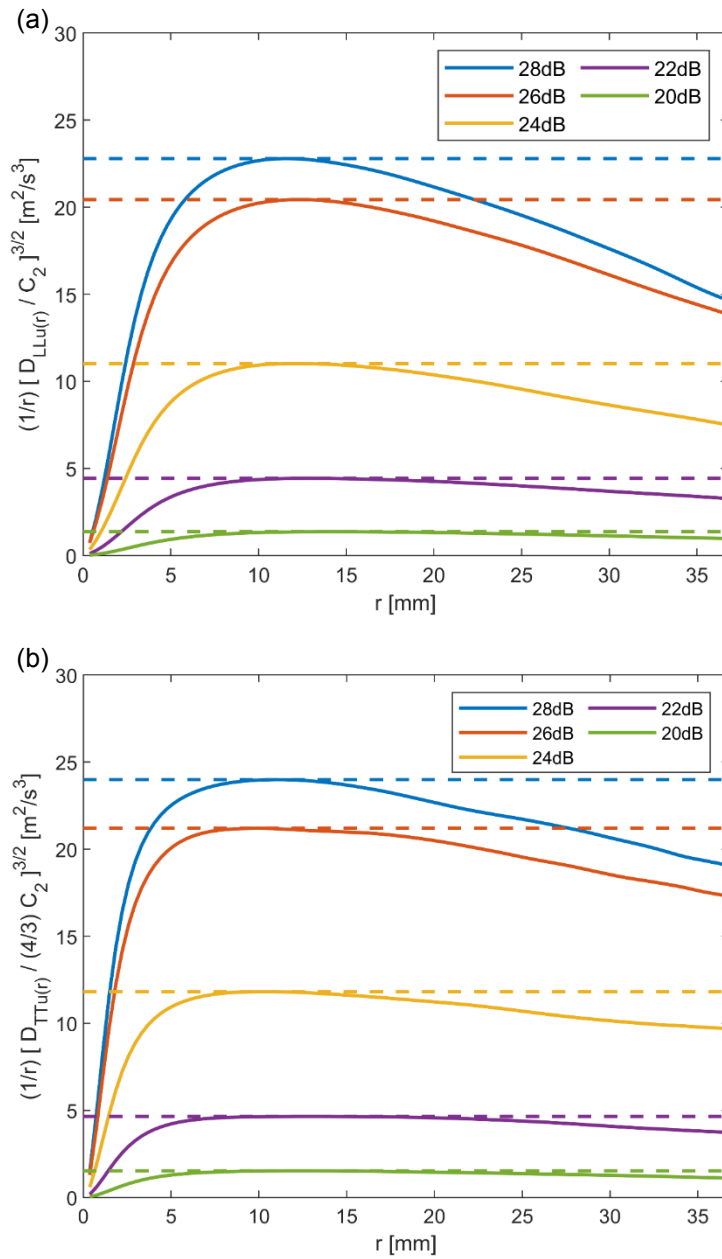


Figure 5.1 Compensated structure functions and the estimated dissipation rate values (case 1-5) (a) Compensated longitudinal SFs (horizontal velocities) (b) Compensated transverse SFs (horizontal velocities)

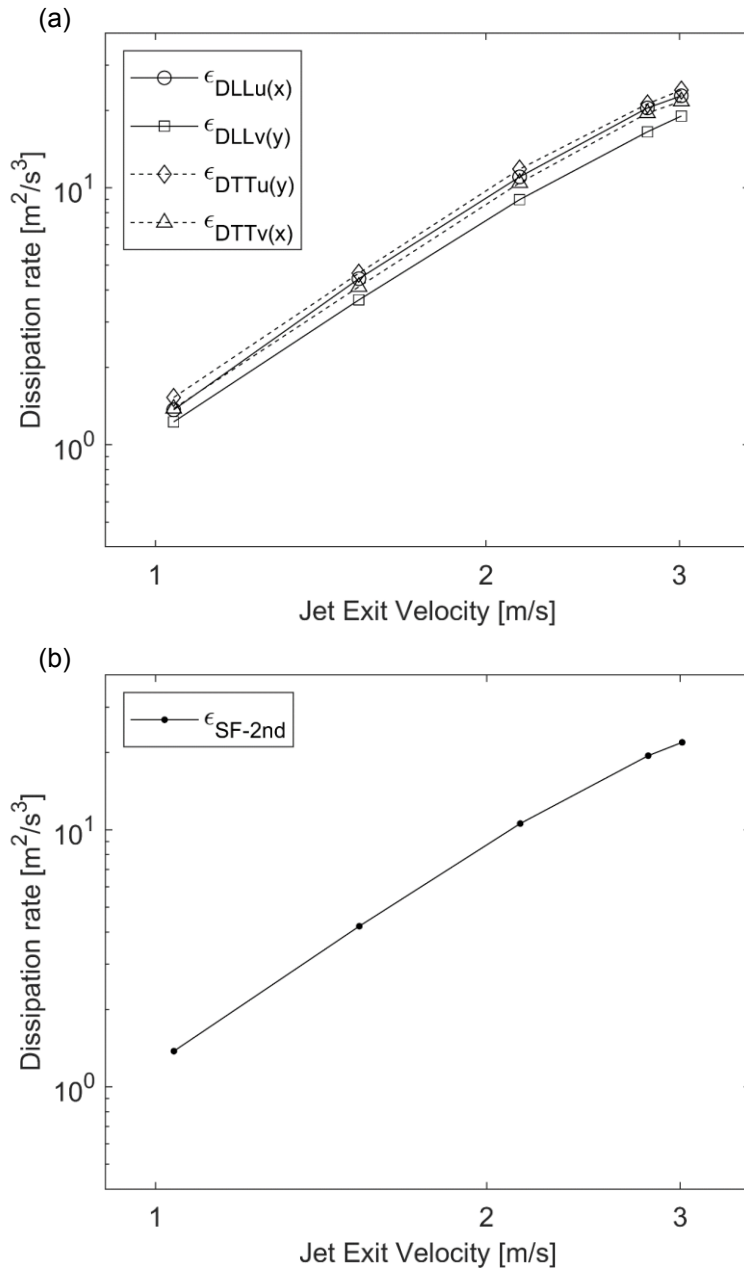


Figure 5.2 Dissipation rate measurement using structure-function fitting method, five points corresponding to case 1 to 5 (a) Dissipation rate from four SFs in the four different directions (b) Averaged quantities over the four values for each condition

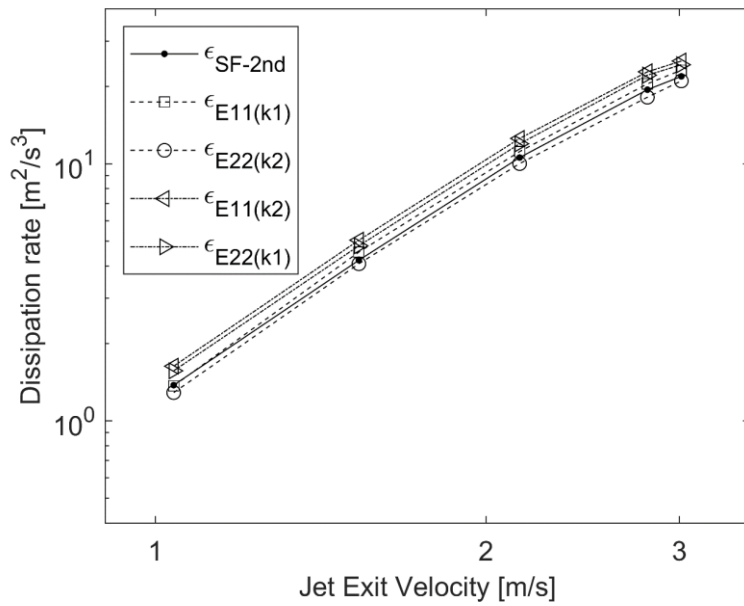


Figure 5.3 Dissipation rate measurement using energy spectra fitting method, five points corresponding to case 1 to 5

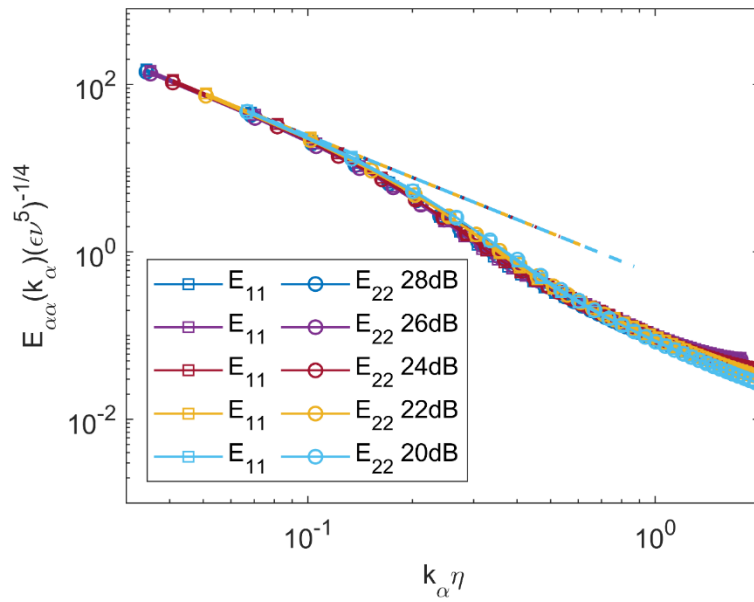


Figure 5.4 Normalized longitudinal 1D energy spectra (case 1 to 5)

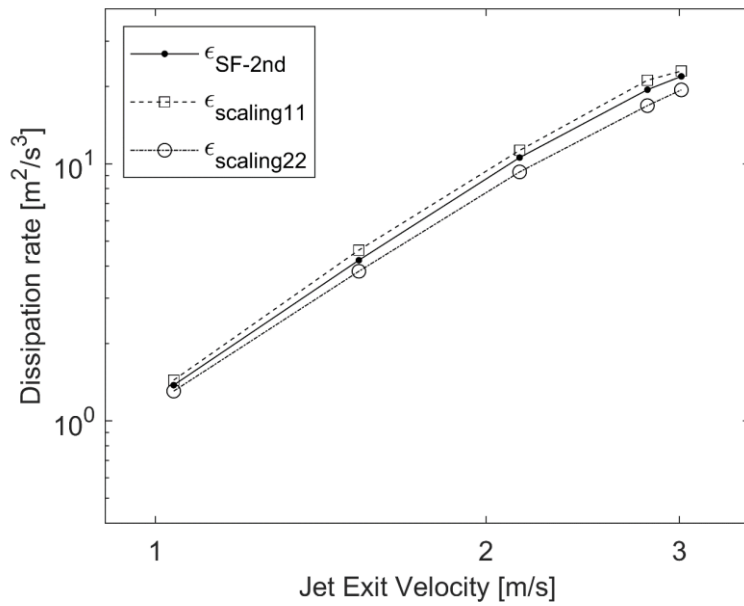


Figure 5.5 Dissipation rate measurement using dissipation scaling method, five points corresponding to case 1 to 5

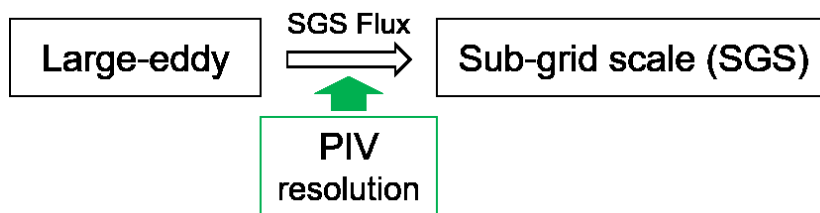


Figure 5.6 Schematic diagram of the large-eddy method adopting a SGS model from large-eddy simulations (LES)

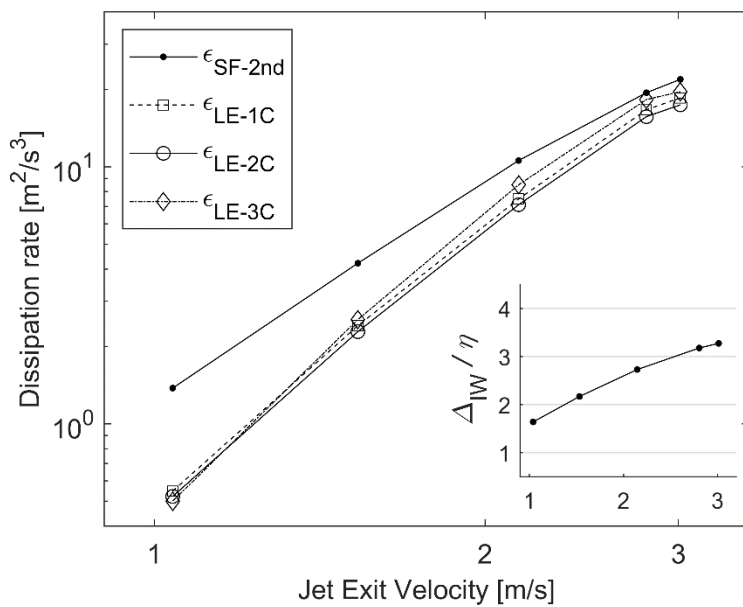


Figure 5.7 Dissipation rate measurement using large eddy method, five points corresponding to case 1 to 5; Inner box is the normalized PIV resolution (Δ_{IW} over η)

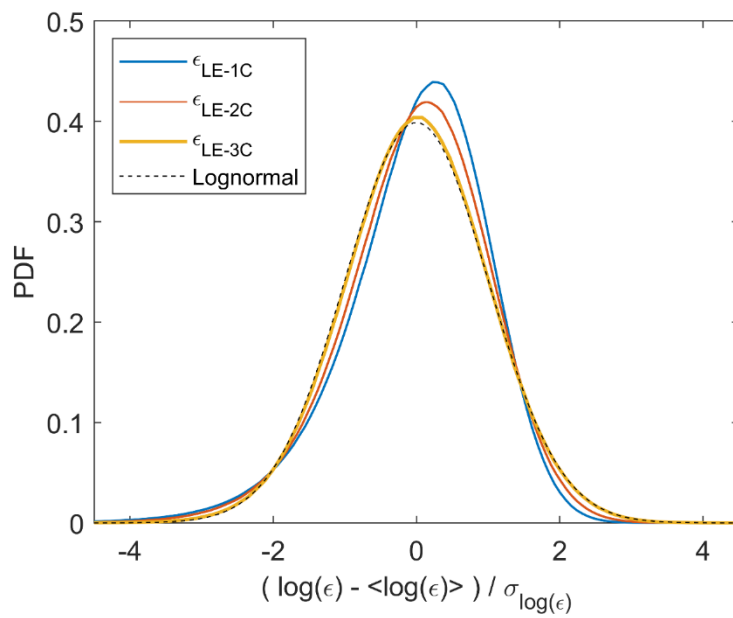


Figure 5.8 Probability density functions of the dissipation rate measured using the large-eddy method (case 1), showing lognormal distribution

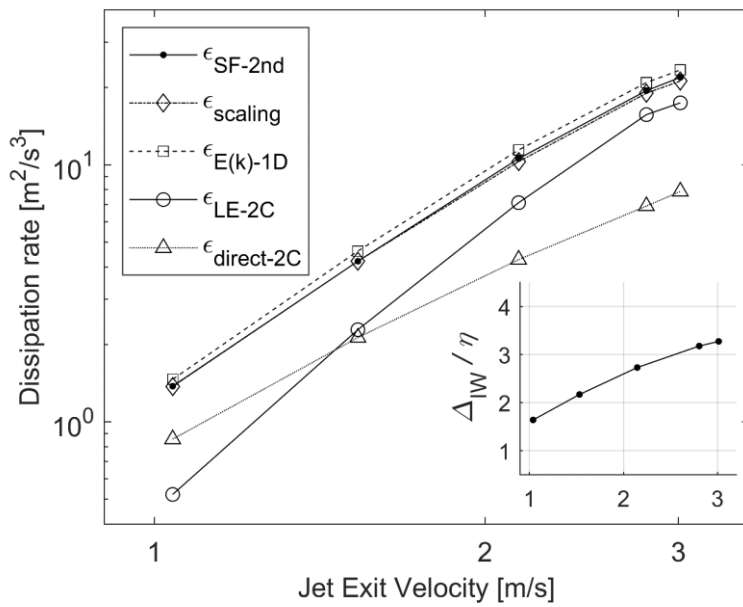


Figure 5.9 Comparison of the dissipation rate measurement using five different methods, five points corresponding to case 1 to 5; Inner box is the normalized PIV resolution (Δ_{IW} over η)

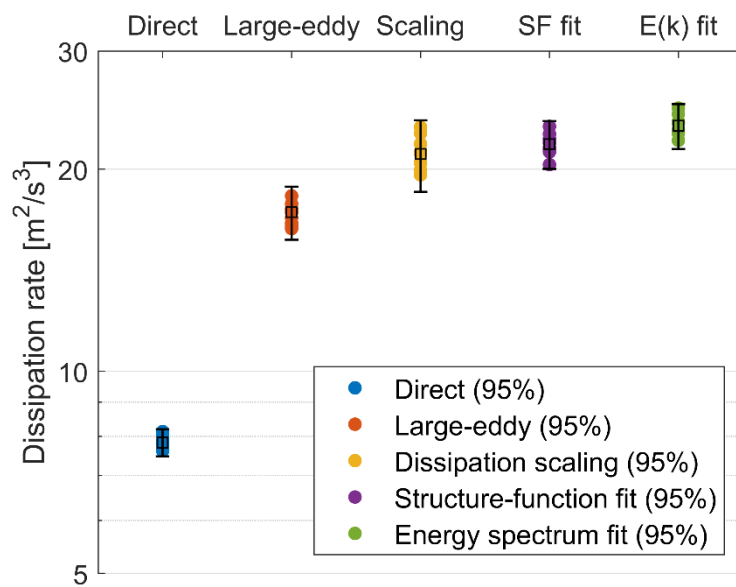


Figure 5.10 Repeatability check for the five methods (for case 1), error bar corresponds to the 95% confidence interval

Chapter 6. Uncertainty Analysis

Although the majority of this thesis utilizes in-plane 3D stereoscopic PIV, many studies are still done using standard 2D PIV. Thus, in this chapter, we quantitatively investigate the random error in standard 2D PIV measurements, and the uncertainty propagation to turbulence statistics from the PIV velocity error, using both analytical and numerical frameworks. The mathematical expectations of the propagated errors under the Gaussian error assumption draw the correction formulas, and the Taylor-series method analytically calculates the resultant uncertainty. With presumed local and instantaneous PIV velocity uncertainty, Monte-Carlo simulations validate both error corrections and uncertainty quantification using a numerical planar PIV model. The expectation value of nonlinear estimates tends to increase due to spurious random fluctuations. The uncertainty value is proportional to the presumed PIV velocity uncertainties, and the proportionality factor reflects the flow structure. The new method proposes simple explicit formulas of error and uncertainty, so that turbulence measurements by PIV can be improved, and reliability of the results can be quantified.

6.1. Literature survey

Particle image velocimetry (PIV) has become a primary experimental method for measuring fluid velocity fields over a wide range of length scales. However, this technique has inherent uncertainty, the magnitude of which can significantly vary depending on the experimental setup, image processing, and flow complexity (Huang *et al.*, 1997; Westerweel, 2000). For example, optical distortions (Reuss *et al.*, 2002), light-sheet misalignment (Grayson *et al.*, 2018), camera saturation, low

particle density, speckles (Scharnowski & Kahler, 2016b), peak-locking (Fincham & Spedding, 1997; Christensen, 2004), sub-grid regression (Roesgen, 2003; Nobach & Honkanen, 2005), time-interval of image-pair (Scharnowski *et al.*, 2019), and spatial resolution limit (Kahler *et al.*, 2012) can be sources of uncertainty. The overall displacement uncertainty of PIV is commonly assumed to be 0.1 pixel, while it can reach as low as 0.05 pixel with precisely controlled experiments, without flow gradients or solid boundaries (Kahler *et al.*, 2016). On the other hand, it can rapidly increase, more than tenfold, in poor conditions such as with considerable out-of-plane motion (Nobach & Bodenschatz, 2009) and aberrations (Reuss *et al.*, 2002).

Within a measurement region, the PIV uncertainty may differ due to an inhomogeneous flow field and non-uniform contributors to error. Moreover, its level is subject to change in time with nonstationary flows. Therefore, many recent studies have focused on quantifying the local and instantaneous uncertainty embedded in PIV results (Timmins *et al.*, 2012; Charonko & Vlachos, 2013; Sciacchitano *et al.*, 2013; Wieneke, 2015; Scharnowski & Kahler, 2016a). However, none of them has been widely accepted as the standard (Sciacchitano *et al.*, 2015; Sciacchitano, 2019). According to these studies, the resulting uncertainty in a single PIV velocity measurement is largely influenced by post-processing. Among these schemes, we employed the image matching method (Sciacchitano *et al.*, 2013) to quantify the PIV random error while using the same turbulence chamber and optical equipment, but one CCD camera for planar PIV, which shows a value of 0.1 to 0.2 px (Jung *et al.*, 2019), agreeing with the literature.

For a certain amount of PIV velocity uncertainty, the propagation of the uncertainty into instantaneous and time-averaged quantities has been investigated using Taylor-series analyses and Monte-Carlo simulations (Wilson & Smith, 2013a). Under the assumption of normally-distributed random error, an experimental study

compared the Taylor-series method with experiments, and then suggested the necessity of correction to nonlinear statistical quantities such as the strain rate invariant (Wilson & Smith, 2013b). Furthermore, uncertainty propagation has been extended to consider spatial correlations and nonlinear statistics, which has been assessed via both experiments and Monte-Carlo simulations (Sciacchitano & Wieneke, 2016).

As discussed in Chapter 5, the dissipation rate ε is one of the essential descriptive parameters of turbulence, as it is key to understanding turbulent length and time scales. Therefore, many researchers have investigated dissipation rate estimation using PIV. Strong dependency on the effect of PIV sub-window size and spatial resolution has been shown by analytical and experimental methods (Saarenrinne & Piirto, 2000; Saarenrinne *et al.*, 2001; Zaripov *et al.*, 2019). Moreover, analytical corrections to the PIV dissipation rate measurements have been suggested because of the limited spatial resolution (Lavoie *et al.*, 2007; Tanaka & Eaton, 2007). However, these studies rely on the direct method (Section 5.1) and use the definition of the dissipation rate, which theoretically requires high spatial resolution to capture the smallest turbulent flow scales. This does not generally apply to typical PIV conditions. In practice, the dissipation rate can be estimated using the large-eddy method (Section 5.5).

Although considerable research has been devoted to estimating uncertainties in PIV and its propagation into basic quantities, rather less attention has been paid to uncertainties in turbulence statistics. Indeed, in measuring turbulent flow, PIV uncertainty can play a more crucial role due to complex fluid motion with high-velocity gradients (Meunier & Leweke, 2003; Li, D. X. *et al.*, 2008; Westerweel, 2008). In this chapter, therefore, we quantify the influence of PIV uncertainty on the dissipation rate ε measurement using the large-eddy method and propose an error

correction to the quantities derived from the PIV dataset.

6.2. Error correction

From now on, planar PIV is considered which measures two velocity components (u_1, u_2) in a planar domain. In PIV, processed statistics contain error that is inherently due to velocity uncertainty. Thus, nonlinearly derived quantities tend to deviate from the true value. This error is first quantified, then corrected in this section. Moreover, the uncertainty propagation is analytically examined, and then numerically assessed using a PIV model in the following sections.

PIV measures a displacement field of working fluid at an instant, and then obtains a velocity field within a specific time interval. The i^{th} -component of the measured displacement Δx_i^e can be decomposed into the true value Δx_i and random error $e_{\Delta x_i}$, where the superscript e denotes the measured value with an error. By dividing the displacement value by a preset time interval Δt , we get the measured velocity in the following form.

$$u_i^e = u_i + e \quad (\text{Eq. 6.1})$$

The error denoted as noise is assumed to be independent, compared to the velocity value itself (Carr *et al.*, 2009), and thus follows a normal distribution with zero mean: $e \sim N(0, \sigma_e^2)$. The standard deviation of the error σ_e corresponds to the standard uncertainty of the velocity measurement. Here, note that the equation does not account for bias error, but only for random error, because bias errors cancel out when dealing with fluctuating components. Moreover, for PIV statistical quantities, random uncertainties, not bias ones, dominate the overall uncertainty (Sciacchitano & Wieneke, 2016). Since all the results that are derived from the PIV velocity contain

the intrinsic velocity error term in Eq. 6.1, the deviation of the results due to the errors can be statistically obtained by calculating the mathematical expectation of the errors. In reverse, by subtracting the deviation from the measured values, corrected results can be found.

First, the correction to the RMS of velocity fluctuation $u_{i,\text{RMS}}$ was examined. Herein, we write $u'_{i,\text{RMS}}$ instead of $u_{i,\text{RMS}}$ for clearly emphasizing “fluctuation,” and we may simply write u instead of u_i for the sake of brevity. Regarding this point, we also need to be reminded that the velocity fluctuation RMS $u'_{i,\text{RMS}}$ is defined as the second moment (standard deviation) of the measured velocities as follows.

$$u_{\text{RMS}}^{e'} = \sigma_{u^e} \quad (\text{Eq.6.2})$$

In the actual measurement, the fluctuation consists of both true turbulent fluctuations and spurious fluctuations from noise. The velocity fluctuation RMS value is overestimated because of this latter noise. The expected value of the measured velocity fluctuation RMS is as follows, where overbar denotes time or ensemble averaging.

$$u^{e'} = u^e - \overline{u^e} = (u_i + e) - (\overline{u_i} + \overline{e}) = u' + e' \quad (\text{Eq.6.3})$$

$$E[u_{\text{RMS}}^{e'}] = \sqrt{u'^2 + E[2e'u' + e'^2]} = \sqrt{u'^2 + \sigma_e^2} \quad (\text{Eq.6.4})$$

It is assumed that the expectation of $\overline{e'u'}$ is equal to zero because the noise and true velocity are independent of each other. Since the PIV uncertainty that corresponds to the uncertainty of velocity measurement has been determined, the velocity fluctuation RMS can be corrected by calculating the inverse function.

$$u'_{\text{RMS}}{}^{\text{corr}} = \sqrt{u'^{\text{e}'}_{\text{RMS}}{}^2 - \sigma_e^2} \quad (\text{Eq.6.5})$$

Second, the correction to the strain rate invariant squared $|s|^2 = 2s'_{ij}s'_{ij}$ (twice that of Eq. 5.6) was examined. Before directly going through the strain rate, we first examine the spatial derivative within the strain rate equation. Finite differencing was used to estimate the spatial derivatives of the velocity fluctuation field, sampled on equidistant grids in order to obtain the velocity fluctuation gradient tensor $\frac{\partial u'_j}{\partial x_i}$. The derivative involves a truncation error, and extensive studies have examined this effect. It has been shown that second-order central differencing is sufficiently accurate, and is thus widely used (Lourenco & Krothapalli, 1995; Foucaut & Stanislas, 2002; Etebari & Vlachos, 2005). Here, the second-order central difference scheme was employed, while the truncation error was not taken into account, as it is beyond the scope of this study. Moreover, when dealing with the dissipation rate measured by the large-eddy method, the truncation error can be analogically interpreted as part of a turbulence model.

The spatial derivative was calculated as follows,

$$\frac{\partial u'_j}{\partial x_i} = \frac{u'^e_j(x_i+\Delta x) - u'^e_j(x_i-\Delta x)}{2\Delta x} = \frac{\partial u'_j}{\partial x_i} + \frac{e_+ - e_-}{2\Delta x}, \quad (\text{Eq.6.6})$$

where Δx denotes the grid spacing and e_{\pm} simply denotes $e_j(x_i \pm \Delta x)$. Since the derivative is a linear function of two errors, its expected value is always equal to the true value. The square of the spatial derivative can also be considered as follows,

$$\left(\frac{\partial u'_j}{\partial x_i}\right)^2 = \left(\frac{\partial u'_j}{\partial x_i}\right)^2 + \left(\frac{e_+ - e_-}{\Delta x}\right) \frac{\partial u'_j}{\partial x_i} + \frac{e_+^2 - 2e_+e_- + e_-^2}{4(\Delta x)^2}, \quad (\text{Eq.6.7})$$

where the expected value of the second term on the right-hand side is zero. From the characteristics of the normal distribution that the square of the random variable has the expected value equal to the variance, $E[e^2] = \sigma_e^2$, and that the correlation of independent random variables is zero, $E[e_+e_-] = 0$, the following holds.

$$E \left[\left(\frac{\partial u_j^{e'}}{\partial x_i} \right)^2 \right] = \left(\frac{\partial u_j'}{\partial x_i} \right)^2 + \frac{1}{2} \left(\frac{\sigma_e}{\Delta x} \right)^2 \quad (\text{Eq.6.8})$$

$$\left(\frac{\partial u_j'}{\partial x_i} \right)^{2,corr} = \left(\frac{\partial u_j^{e'}}{\partial x_i} \right)^2 - \frac{1}{2} \left(\frac{\sigma_e}{\Delta x} \right)^2 \quad (\text{Eq.6.9})$$

The strain rate tensor invariant squared $|s|^{e2} = 2s_{ij}^e s_{ij}^e$ can be rewritten, from Eq. 5.6, as follows, where this one quantity needs eight independent measurements of velocity components.

$$\begin{aligned} |s|^{e2} = & 4 \left(\frac{\partial u_1^{e'}}{\partial x_1} \right)^2 + 4 \left(\frac{\partial u_2^{e'}}{\partial x_2} \right)^2 + 3 \left(\frac{\partial u_1^{e'}}{\partial x_2} \right)^2 + 3 \left(\frac{\partial u_2^{e'}}{\partial x_1} \right)^2 + \\ & 4 \left(\frac{\partial u_1^{e'}}{\partial x_1} \frac{\partial u_2^{e'}}{\partial x_2} \right) + 6 \left(\frac{\partial u_1^{e'}}{\partial x_2} \frac{\partial u_2^{e'}}{\partial x_1} \right) \end{aligned} \quad (\text{Eq.6.10})$$

As seen in Eq. 6.8, the first four terms are expected to be overestimated by $\frac{1}{2}(\sigma_e/\Delta x)^2$ times its coefficient. Since the last two terms only have linear components of the random error, their expectations equal the true values. Therefore, the expected and corrected values of resolved strain rate invariant squared were derived as follows.

$$E[|s|^{e2}] = |s|^2 + 7 \left(\frac{\sigma_e}{\Delta x} \right)^2 \quad (\text{Eq.6.11})$$

$$|s|^{2,corr} = |s|^{e^2} - 7 \left(\frac{\sigma_e}{\Delta x} \right)^2 \quad (\text{Eq.6.12})$$

Third and last, the correction to the dissipation rate measurement using the large-eddy method was examined. The large-eddy method can be rewritten as follows, which is exactly the same as Eq. 5.15.

$$\varepsilon_{LE}^e = C_s^2 \Delta_{IW}^2 (|s|^{e^2})^{3/2} \quad (\text{Eq.6.13})$$

Because this quantity is a complicated multivariate function including the square-root-sum of random variables, its mathematical expectation cannot reduce to a closed-form expression. Therefore, the quadratic Taylor series approximation was first applied, and then the expectation value was approximately calculated. The dissipation rate, a function of eight independent errors, can be written as

$$\varepsilon_{LE}^e = \varepsilon_{LE}^e(e_n) \quad (n = 1, 2, \dots, 8), \quad (\text{Eq.6.14})$$

where e_n denotes each of the eight errors, and the expectation of the Taylor series approximation is calculated as follows.

$$E[\varepsilon_{LE}^e] = \varepsilon_{LE}^e + E \left[\frac{1}{2!} \sum_{n=1}^8 \left(\frac{\partial^2 \varepsilon_{LE}^e}{\partial e_n^2} \right)_{e=0} e_n^2 \right] \quad (\text{Eq.6.15})$$

Note that the expected values of the first-order terms and the second-order correlation terms were excluded because they have zero value, as errors are normally distributed and independent, thus leaving only the squared terms. The second derivative of the measured dissipation rate is

$$\left(\frac{\partial^2 \varepsilon_{LE}^e}{\partial e_n^2} \right)_{e=0} = \frac{3}{4} C_s^2 \Delta_{IW}^2 \left\{ |s|^{-1} \left(\frac{\partial |s|^{e^2}}{\partial e_n} \right)^2 + 2|s| \left(\frac{\partial^2 |s|^{e^2}}{\partial e_n^2} \right) \right\}_{e=0}, \quad (\text{Eq.6.16})$$

and its substitution into Eq.6.15 yields the following.

$$E[\varepsilon_{LE}^e] = \varepsilon_{LE} + \frac{3}{8} C_S^2 \Delta_{IW}^2 |s|^{-1} E \left[\sum_{n=1}^8 \left(\frac{\partial |s| e^2}{\partial e_n} \right)_{e_n=0}^2 e_n^2 \right] + \frac{3}{4} |s| E \left[\sum_{n=1}^8 \left(\frac{\partial^2 |s| e^2}{\partial e_n^2} \right)_{e_n=0} e_n^2 \right] \quad (\text{Eq.6.17})$$

Each derivative can be obtained from Eq.6.10, and each expectation value of error squared can be obtained using the normal error assumption, $E[e^2] = \sigma_e^2$. Then we find the approximate expectation and the correction of the dissipation rate using the large-eddy PIV method as follows.

$$E[\varepsilon_{LE}^e] = \varepsilon_{LE} + \frac{3}{2} C_S^2 \Delta_{IW}^2 \left\{ |s|^{-1} \left[10 \left(\frac{\partial u'_1}{\partial x_1} \right)^2 + 10 \left(\frac{\partial u'_2}{\partial x_2} \right)^2 + 16 \left(\frac{\partial u'_1}{\partial x_1} \frac{\partial u'_2}{\partial x_2} \right) + 9 \left(\frac{\partial u'_1}{\partial x_2} + \frac{\partial u'_2}{\partial x_1} \right)^2 \right] + 7|s| \right\} \left(\frac{\sigma_e}{\Delta x} \right)^2 \quad (\text{Eq.6.18})$$

$$\varepsilon_{LE}^{corr} = \varepsilon_{LE}^e - \frac{3}{2} C_S^2 \Delta_{IW}^2 \left\{ |s|^{e-1} \left[10 \left(\frac{\partial u_1^{e'}}{\partial x_1} \right)^2 + 10 \left(\frac{\partial u_2^{e'}}{\partial x_2} \right)^2 + 16 \left(\frac{\partial u_1^{e'}}{\partial x_1} \frac{\partial u_2^{e'}}{\partial x_2} \right) + 9 \left(\frac{\partial u_1^{e'}}{\partial x_2} + \frac{\partial u_2^{e'}}{\partial x_1} \right)^2 \right] + 7|s|^e \right\} \left(\frac{\sigma_e}{\Delta x} \right)^2 \quad (\text{Eq.6.19})$$

6.3. Uncertainty propagation

In order to quantify the uncertainty in an experimental result that is a multivariate function of J -variables, the Taylor-series method (TSM) is used (Coleman & Steele, 2018). For the result $r = r(X_1, X_2, \dots, X_J)$, this method gives the uncertainty as follows, where $U[X_i]$ denotes the uncertainty of the measured value X_i .

$$U^2[r] = \left(\frac{\partial r}{\partial x_1}\right)^2 U^2[X_1] + \left(\frac{\partial r}{\partial x_2}\right)^2 U^2[X_2] + \dots + \left(\frac{\partial r}{\partial x_j}\right)^2 U^2[X_j] \quad (\text{Eq.6.20})$$

When the uncertainties of statistical quantities are obtained from a set of samples $x = \{x_1, x_2, \dots, x_N\}$, the estimation of the mean and variance from the measured sample data are defined, respectively, as follows.

$$\bar{x} = \frac{1}{N} \sum_{i=1}^N x_i \quad (\text{Eq.6.21})$$

$$\sigma_x^2 = \frac{1}{N-1} \sum_{i=1}^N (x_i - \bar{x})^2 \quad (\text{Eq.6.22})$$

The standard uncertainty is defined as an estimate of the standard deviation of the parent population from which a particular elemental error originates [36]. By the definitions, therefore, the standard uncertainty is equal to the estimated standard deviation. Moreover, the 95% uncertainty corresponds to the 95% confidence level, which means 95% of error is expected to lie in the interval based on the Student's t -distribution. The 95% uncertainty value is obtained by multiplying the standard uncertainty and the 95% t -statistic of the sample size N . For averaged quantities, since we assumed that independent samples follow a distribution of standard deviation σ_x , the standard uncertainty of the average is given as follows (Benedict & Gould, 1996).

$$U[\bar{x}] = \frac{\sigma_x}{\sqrt{N}} \quad (\text{Eq.6.23})$$

First, the standard uncertainty of the velocity fluctuation RMS was obtained using the TSM as follows, where the standard uncertainty of a Gaussian random variable equals the standard deviation: $U[e] = \sigma_e$.

$$\begin{aligned}
U^2[u_{RMS}^{e'}] &= U^2 \left[\sqrt{\frac{1}{N} \sum_{i=1}^N (u'_i + e'_i)^2} \right] \\
&= \left(\frac{1}{2u_{RMS}^{e'}} \right)^2 U^2 \left[\frac{1}{N} \sum_{i=1}^N (u'_i + e'_i)^2 \right] \\
&= \frac{1}{4u_{RMS}^{e'2}} \frac{1}{N^2} \sum_{i=1}^N \{ [2(u'_i + e'_i)]^2 U^2[e'_i] \} \\
&= \frac{1}{u_{RMS}^{e'2}} \frac{1}{N^2} \sum_{i=1}^N (u'_i + e'_i)^2 \sigma_e^2 = \frac{\sigma_e^2}{N} \quad (\text{Eq.6.24})
\end{aligned}$$

$$U[u_{RMS}^{e'}] = \frac{\sigma_e}{\sqrt{N}} \quad (\text{Eq.6.25})$$

As the variance of the error itself is negligible compared to the variance of velocity measurement with the error model that assumes a fixed error variance, the uncertainty of the corrected value becomes nearly the same as the standard uncertainty without correction (Sciacchitano & Wieneke, 2016).

$$U[u_{RMS}^{e'corr}] \approx U[u_{RMS}^{e'}] \quad (\text{Eq.6.26})$$

This assumption can be applied to all the following corrected values; thus the uncertainties of corrected values will not be derived separately.

Second, the standard uncertainty of the strain rate invariant squared was obtained. The strain rate invariant square, Eq.6.10, can be rewritten in another form to separate longitudinal and transverse components as follows.

$$|s|^{e2} = 4 \left\{ \left(\frac{\partial u_1^{e'}}{\partial x_1} \right)^2 + \left(\frac{\partial u_2^{e'}}{\partial x_2} \right)^2 + \left(\frac{\partial u_1^{e'}}{\partial x_1} \frac{\partial u_2^{e'}}{\partial x_2} \right) \right\} + 3 \left(\frac{\partial u_1^{e'}}{\partial x_2} + \frac{\partial u_2^{e'}}{\partial x_1} \right)^2 \quad (\text{Eq.6.27})$$

As the uncertainties in the first term and the second term are independent, we use

Eq.6.20 to obtain the overall uncertainty:

$$U^2[|s|e^2] = 16U^2 \left[\left(\frac{\partial u_1^{e'}}{\partial x_1} \right)^2 + \left(\frac{\partial u_2^{e'}}{\partial x_2} \right)^2 + \left(\frac{\partial u_1^{e'}}{\partial x_1} \frac{\partial u_2^{e'}}{\partial x_2} \right) \right] + 9U^2 \left[\left(\frac{\partial u_1^{e'}}{\partial x_2} + \frac{\partial u_2^{e'}}{\partial x_1} \right)^2 \right]. \quad (\text{Eq.6.28})$$

Applying the uncertainty propagation formula (Eq.6.10), where each term consists of four measured variables with the corresponding errors as seen in Eq. 6.6, we obtained the standard uncertainty of the strain rate invariant squared:

$$U[|s|e^2] = 2 \sqrt{10 \left(\frac{\partial u_1^{e'}}{\partial x_1} \right)^2 + 10 \left(\frac{\partial u_2^{e'}}{\partial x_2} \right)^2 + 16 \left(\frac{\partial u_1^{e'}}{\partial x_1} \frac{\partial u_2^{e'}}{\partial x_2} \right) + 9 \left(\frac{\partial u_1^{e'}}{\partial x_2} + \frac{\partial u_2^{e'}}{\partial x_1} \right)^2} \left(\frac{\sigma_e}{\Delta x} \right). \quad (\text{Eq.6.29})$$

When measuring stationary turbulent flow, the time-averaged statistical quantity is normally used. From Eq.6.23 the standard uncertainty of the temporal average over N samples is:

$$U \left[\overline{|s|e^2} \right] = \frac{2}{\sqrt{N}} \sqrt{10 \left(\overline{\frac{\partial u_1^{e'}}{\partial x_1}} \right)^2 + 10 \left(\overline{\frac{\partial u_2^{e'}}{\partial x_2}} \right)^2 + 16 \left(\overline{\frac{\partial u_1^{e'}}{\partial x_1} \frac{\partial u_2^{e'}}{\partial x_2}} \right) + 9 \left(\overline{\frac{\partial u_1^{e'}}{\partial x_2} + \frac{\partial u_2^{e'}}{\partial x_1}} \right)^2} \left(\frac{\sigma_e}{\Delta x} \right), \quad (\text{Eq.6.30})$$

where the over-line denotes temporally averaged quantity. Here, the magnitude of PIV uncertainty is assumed to be stationary with time.

The third is the standard uncertainty of the dissipation rate measurement using the large-eddy method. This value can be derived from Eq.6.28, by applying the uncertainty propagation formula Eq.6.20.

$$\begin{aligned}
U^2[\varepsilon_{LE}^e] &= \left(\frac{\partial \varepsilon_{LE}^e}{\partial |s|e^2} \right)^2 U^2[|s|e^2] \\
&= \left\{ \frac{3}{2} C_s^2 \Delta^2 (|s|e^2)^{\frac{1}{2}} \right\}^2 U^2[|s|e^2] = \frac{9}{4} \{C_s^2 \Delta^2\}^2 \left(\frac{\varepsilon_{LE}^e}{C_s^2 \Delta^2} \right)^{\frac{2}{3}} U^2[|s|e^2] \\
&= 9(C_s^2 \Delta^2)^{\frac{4}{3}} (\varepsilon_{LE}^e)^{\frac{2}{3}} \left\{ 10 \left(\frac{\partial u_1^{e'}}{\partial x_1} \right)^2 + 10 \left(\frac{\partial u'}{\partial x_2} \right)^2 + 16 \left(\frac{\partial u_1^{e'}}{\partial x_1} \frac{\partial u_2^{e'}}{\partial x_2} \right) + 9 \left(\frac{\partial u_1^{e'}}{\partial x_2} + \frac{\partial u_2^{e'}}{\partial x_1} \right)^2 \right\} \left(\frac{\sigma_e}{\Delta x} \right)^2
\end{aligned} \tag{Eq.6.31}$$

Thus, the standard uncertainty of the dissipation rate is reduced into the following form.

$$U[\varepsilon_{LE}^e] = 3(C_s^2 \Delta^2)^{\frac{2}{3}} (\varepsilon_{LE}^e)^{\frac{1}{3}} \sqrt{10 \left(\frac{\partial u_1^{e'}}{\partial x_1} \right)^2 + 10 \left(\frac{\partial u'}{\partial x_2} \right)^2 + 16 \left(\frac{\partial u_1^{e'}}{\partial x_1} \frac{\partial u_2^{e'}}{\partial x_2} \right) + 9 \left(\frac{\partial u_1^{e'}}{\partial x_2} + \frac{\partial u_2^{e'}}{\partial x_1} \right)^2} \left(\frac{\sigma_e}{\Delta x} \right) \tag{Eq.6.32}$$

As the same in Eq.6.30, when measuring stationary turbulence, the standard uncertainty of the time-averaged dissipation rate over N samples becomes as follows.

$$U[\varepsilon_{LE}^e] = \frac{3}{\sqrt{N}} (C_s^2 \Delta^2)^{\frac{2}{3}} \sqrt{(\varepsilon_{LE}^e)^{\frac{2}{3}} \left\{ 10 \left(\frac{\partial u_1^{e'}}{\partial x_1} \right)^2 + 10 \left(\frac{\partial u'}{\partial x_2} \right)^2 + 16 \left(\frac{\partial u_1^{e'}}{\partial x_1} \frac{\partial u_2^{e'}}{\partial x_2} \right) + 9 \left(\frac{\partial u_1^{e'}}{\partial x_2} + \frac{\partial u_2^{e'}}{\partial x_1} \right)^2 \right\} \left(\frac{\sigma_e}{\Delta x} \right)^2} \tag{Eq.6.33}$$

6.4. Numerical verification

The Monte-Carlo method is a powerful approach to uncertainty quantification of an experimental result that is a function of measured variables. It draws errors from a Gaussian distribution that formulates a pre-quantified PIV uncertainty, and simulates the measurement repeatedly with individual errors sampled each time. Then, based on the distribution of the collected results, the uncertainty is statistically

determined (Coleman & Steele, 2018). Although the solution is only numerically available for this method, this gives the solution that is closer to the true value for not neglecting high-order terms, contrary to the TSM.

Prior to the statistical evaluation, the PIV measurement was modeled with a three-dimensional velocity field from a direct numerical simulation (DNS) dataset. The Johns Hopkins Turbulence Database (JHTDB) offers a dataset of homogeneous isotropic turbulence (HIT) calculated using DNS, which consists of 1024^3 nodes and 5028 time steps, covering twice the integral length scale and five times the large eddy turnover time, respectively (Li, Y. *et al.*, 2008). Because the DNS dataset contains the true value of each measurement, the PIV model is highly advantageous with respect to exact verification.

PIV measurement is essentially spatial filtering as it obtains one representative velocity over a finite sub-window region. Therefore, a single PIV measurement can be modeled by applying spatial filters to a DNS velocity field. For convenience, the direction perpendicular to the laser sheet is denoted by direction 3, and parallel directions are denoted by direction 1 and 2. In direction 3, Gaussian filtering was applied, due to the intensity distribution of the laser sheet. In direction 1 and 2, top-hat filtering was applied, due to uniform laser intensity over the square sub-window. Normal random error was then added to each sub-window, the magnitude of which was determined from the pre-quantified PIV uncertainty.

For one snapshot of turbulence, two in-plane velocity components at $1024 \cdot 1024 \cdot 65$ nodes for each direction was downloaded. Here, the center of the laser sheet in direction 3 was set to have node number 33. As only discrete data was available, instead of using a Gaussian filtering function for continuous data, a weight function W_j in the definite integral form was applied as follows, where j denotes the node number from 1 to 65 and i denotes the direction 1 and 2.

$$W_j = \frac{1}{2} \operatorname{erf} \left(\sqrt{6} \frac{j+\frac{1}{2}}{\Delta_{sheet}} \right) - \frac{1}{2} \operatorname{erf} \left(\sqrt{6} \frac{j-\frac{1}{2}}{\Delta_{sheet}} \right) \quad (\text{Eq.6.34})$$

$$u_i = \sum_{j=1}^{65} W_{(j-33)} u_{ij} \quad (\text{Eq.6.35})$$

Top-hat filtering was conducted by simply averaging over the square sub-window whose filter size is defined as the length of one side of the square. The filtered grid size was determined according to the overlap ratio. If the overlap ratio is 50% for example, the grid size should be half of the filter size. Finally, a random error e that follows a normal distribution with zero mean and a certain amount of standard deviation σ_e was added to each sub-window individually. A parameter ζ was introduced, which is defined as the ratio of the standard deviation of velocity error to the root-mean-square of overall velocities in the DNS dataset: $\zeta = \sigma_e / (u_{\text{RMS,DNS}})$. This parameter shows the magnitude of PIV uncertainty and its range was assumed to be from 0 to 20%, which is on par with the range of true PIV uncertainty. Here, ζ nominally has a value less than 10% (0.2 px error over 2 px RMS displacement), while it can be as high as 20% in cases of severe optical distortions (Reuss *et al.*, 2002). Finally, one velocity field data set was obtained from the PIV model simulating the laser sheet intensity, sub-window correlation, and measurement error.

The PIV model utilized the filtered DNS dataset instead of the synthetic PIV dataset, because of the limitations of synthetic PIV. Synthetic PIV first generates virtual particle images and implements the PIV software with these images, and thus is dependent on the performance of the PIV software, which is not directly quantifiable. Therefore, we directly added Gaussian error to each velocity value, which comprehensively simulates overall error contributors such as optical constraints, software inaccuracies, or limitations in capturing the flow.

With the given conditions including filter size, overlap ratio, and PIV

uncertainty for time and space, error and uncertainty in the results derived from the PIV measurement can be numerically calculated via the Monte-Carlo Method with the PIV model. One thousand iterations were conducted for each quantity, such as velocity fluctuation RMS, resolved strain rate invariant, dissipation rate, and their corrections. For statistical quantities, the ensemble average over one hundred frames was conducted ahead of the iteration ($N_{\text{frame}} = 100$). The process is depicted in Figure 6.1, where the left part describes the PIV model with input variables that are underlined, and the right part describes Monte-Carlo simulation for a range of PIV uncertainty ($\zeta = 0 - 20\%$). Finally, for the verification, the analytical solutions were compared with the Monte-Carlo solutions.

6.5. Results and discussion

In this section, the analytical approaches to both mathematical expectations (Section 6.2) and uncertainty propagations (Section 6.3) were verified by comparing them to Monte-Carlo results generated by the PIV model (Section 6.4). Then the corrections were validated in the same way.

First, the Monte-Carlo process for the dissipation rate was repeated until its mean value sufficiently converged. Figure 6.2 shows the root-mean-square (RMS) of relative error between the numerical result and analytical estimation for the mean dissipation rate versus iteration number for the case of $\zeta = 10\%$. As can be seen, the relative error definitely decreases with increasing iteration number up to one thousand, while it remains nearly unchanged afterward. Therefore, convergence is achieved at approximately $N_t = 1,000$ for the current simulation, and all of the following simulations hereinafter will have the same iteration number. However, the relative error does not approach zero, but has a residual error rate of 0.0102. This is

because of the inaccuracies involved with second-order approximation in estimating the dissipation rate (Eq.6.15). The subgraph shows that the difference between the relative error and the converged value approaches zero, thus confirming convergence.

The comparison of analytical estimations and Monte-Carlo solutions in terms of mean value within the range of PIV uncertainty are illustrated in Figure 6.3. Note that this illustration presents only one sub-window for the case of $\Delta_{IW} = 32$ and 50% overlap. Figure 6.3(a) and 6.3(b) shows the measurement of velocity fluctuation RMS and the strain rate invariant squared, respectively. Both analytical and numerical means follow each other closely in parabolic form. Figure 6.3(c) shows the dissipation rate measurement, where the approximate mean follows the Monte-Carlo results, but the approximation slightly underestimates with larger PIV uncertainty. The relative errors between the analytical dissipation rate mean values and the numerical values over all the sub-windows in the case of $\xi = 10, 20\%$ is given as a histogram in Figure 6.4. The histogram shows that the RMS relative error was less than 1% for $\xi = 10\%$, and 7.41% for $\xi = 20\%$, which means that the approximation was sufficiently accurate for the smaller PIV uncertainty case, but became inaccurate as the PIV uncertainty increases. This approximation is still practically valid, however, because the actual PIV uncertainty is lower than 10% in general, and it could be improved by considering higher terms in the Taylor-series approximation.

Figure 6.3(c) also shows that, apart from the random error and uncertainty, the dissipation rate measured by PIV differs from that measured by the direct method with full resolution which corresponds to the true value. This is because of the fundamental limit of the large-eddy PIV method, for which the turbulence model in LES (Eq.5.14-15) is responsible. The discrepancy is inevitable, unless PIV spatial resolution is sufficiently fine to capture the smallest dissipative eddies.

Figure 6.5 presents the 95% uncertainty for the three measurements in Figure 6.3. It shows that both analytical and numerical solutions agree well in the region of relatively low PIV uncertainty. However, as the PIV uncertainty increases, both nonlinear contributions and overestimation become considerable; thus the two solutions start to disagree. This demonstrates the limitation of the Taylor-series method, which accounts only for the linear part of the uncertainty propagation.

To verify the correction, the same procedure was conducted with the corrected formulas at the same measurement conditions. Figure 6.6 shows both the non-corrected and the corrected measurements of mean value, where the former ones are taken from Figure 6.3. As can be seen, the overestimation problem in nonlinear measurements due to PIV random uncertainty has been clearly solved. In Figure 6.6(c), a small amount of residual error resulting from the approximation still remains. This was already illustrated in Figure 6.4, and is relatively small compared to the overestimation bias. Moreover, the uncertainty values of the corrected measurement are depicted in Figure 6.5, and it validates the assumption that the uncertainty difference between corrected and non-corrected measurements is negligible.

Figure 6.7 gives the dissipation rate measurements at a certain y location, and demonstrates the effectiveness of the correction. Without the correction, shown as triangular markers, the PIV measurement overestimated the dissipation rate by up to about double in the case of $\zeta = 20\%$. After the correction, on the other hand, the PIV measurement was highly improved, as it approached the error-free PIV dissipation rate value. In the case of $\zeta = 20\%$, some residual error remains, resulting from the second-order approximation, while nearly no residual remains for $\zeta = 10\%$, which agrees with Figure 6.4 and 6.6. The discrepancy between the PIV measurement and DNS direct measurement, regardless of error, is because of the limitation of

turbulence modeling.

In summary, the present work in Chapter 6 has proposed a mathematical framework for the correction of overestimation, resulting from nonlinear propagation of velocity uncertainty embedded in PIV measurements. The framework relies upon the assumption of Gaussian random error and the theory of mathematical expectation. It uses Taylor-series approximation if no exact expectation exists because of complicated error propagation. Monte-Carlo simulations have numerically verified the analytical framework, and overall results indicate that the proposed corrections have largely reduced the inaccuracy in obtaining nonlinear values such as velocity fluctuation RMS, strain rate invariant, and turbulent dissipation rate. The approximation has a relative error RMS of 0.8% for $\zeta = 10\%$ and 7.4% for $\zeta = 20\%$, which means it becomes erroneous with increasing PIV uncertainty, but is still practically valid for typical PIV uncertainties.

Another mathematical framework for the quantification of the propagated uncertainty (Sciacchitano & Wieneke, 2016) has been applied to the values derived from PIV measurement. The framework is based on the pre-determined velocity uncertainty in PIV measurements and its linear propagation. The Monte-Carlo simulations have also numerically assessed the uncertainty propagation, and both results confirm that the framework can quantify the resultant uncertainty. The framework becomes imprecise with increasing PIV uncertainty, because it only accounts for the linear propagation, but the method is still valid for an actual case of PIV uncertainty lower than 10%.

Moreover, a PIV model using the DNS velocity dataset has been suggested for the numerical simulation. The model considers the intensity profile of the laser sheet, spatial filtering over sub-windows, and measurement random errors. This filtered PIV dataset is more appropriate than the synthetic PIV dataset that is widely used,

because it is independent of PIV image processing, and an arbitrary error can be added according to the purpose of simulation. The PIV model can be applied to other simulations of PIV measurement, in lieu of synthetic PIV.

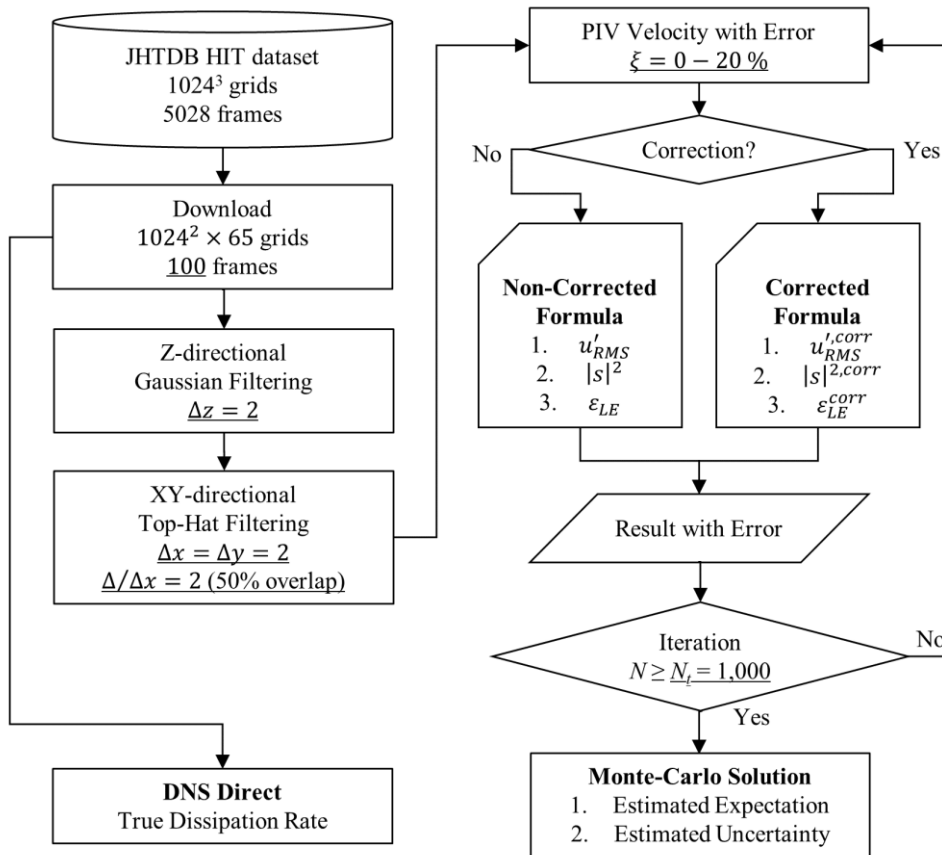


Figure 6.1 Flow chart of Monte-Carlo method using the PIV model with a DNS dataset

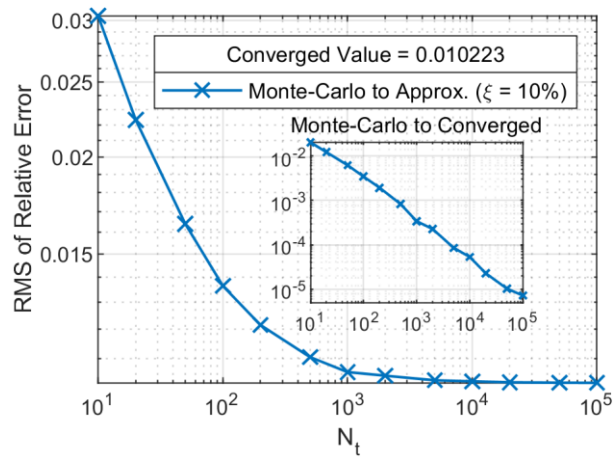


Figure 6.2 Convergence of Monte-Carlo results for the mean corrected dissipation rate ($N_{\text{frame}} = 100$, $\Delta_{\text{IW}} = 32$, 50% overlap)

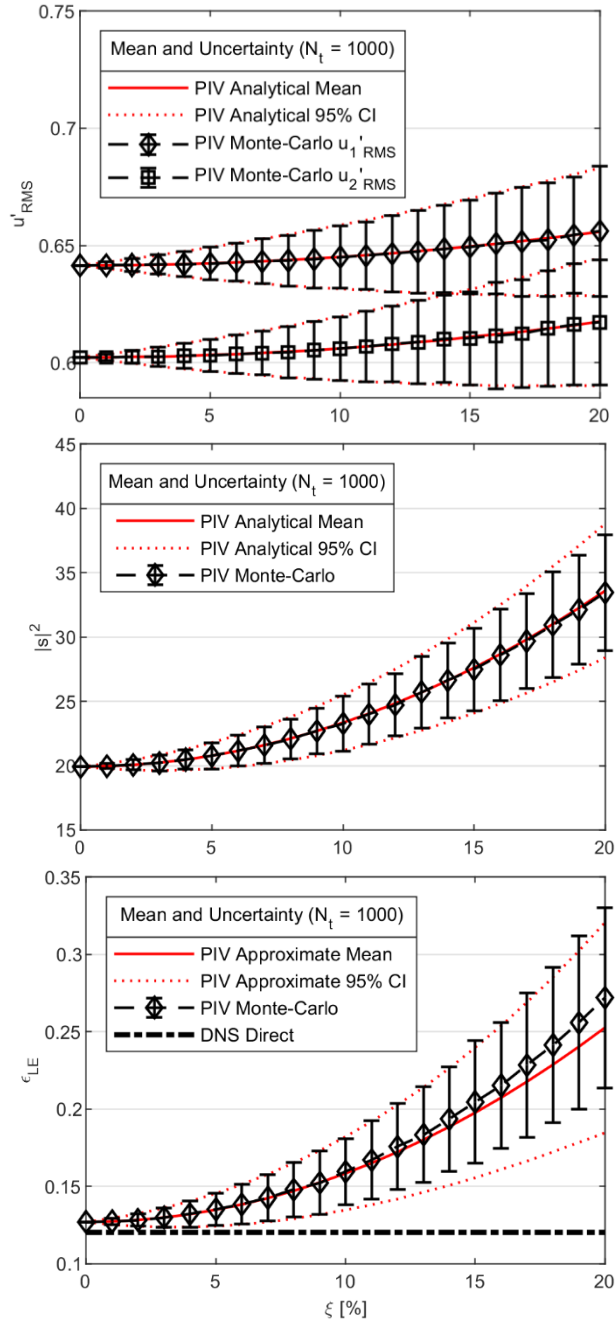


Figure 6.3 Comparison of analytical estimation and Monte-Carlo results for 95% uncertainty value ($N_{frame} = 100$, $\Delta_{IW} = 32$, 50% overlap, (32nd, 8th) sub-window) (a) velocity fluctuation RMS (b) strain rate invariant squared (c) dissipation rate

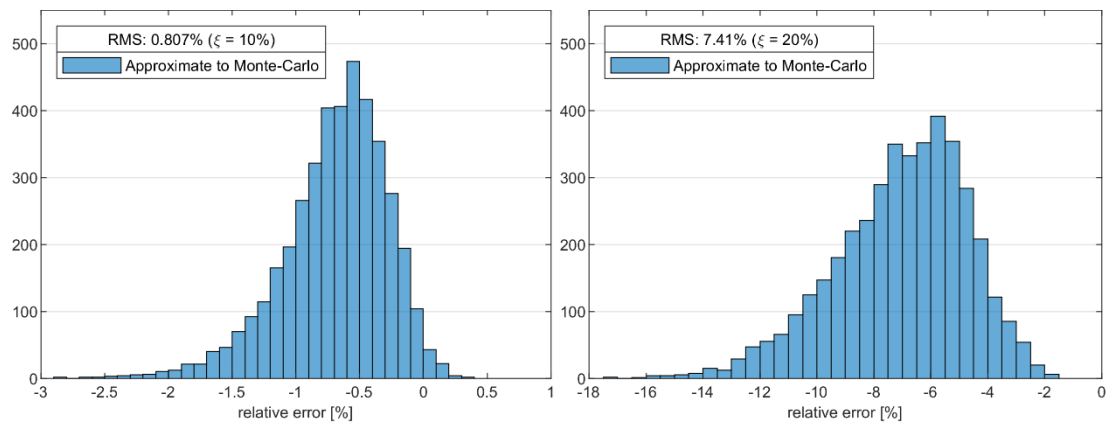


Figure 6.4 Histogram of relative error between approximate solution and Monte-Carlo results for dissipation rate mean value ($N_{\text{frame}} = 100$, $\Delta_{IW} = 32$, 50% overlap, $N_t = 1,000$) (a) $\xi = 10\%$ (b) $\xi = 20\%$

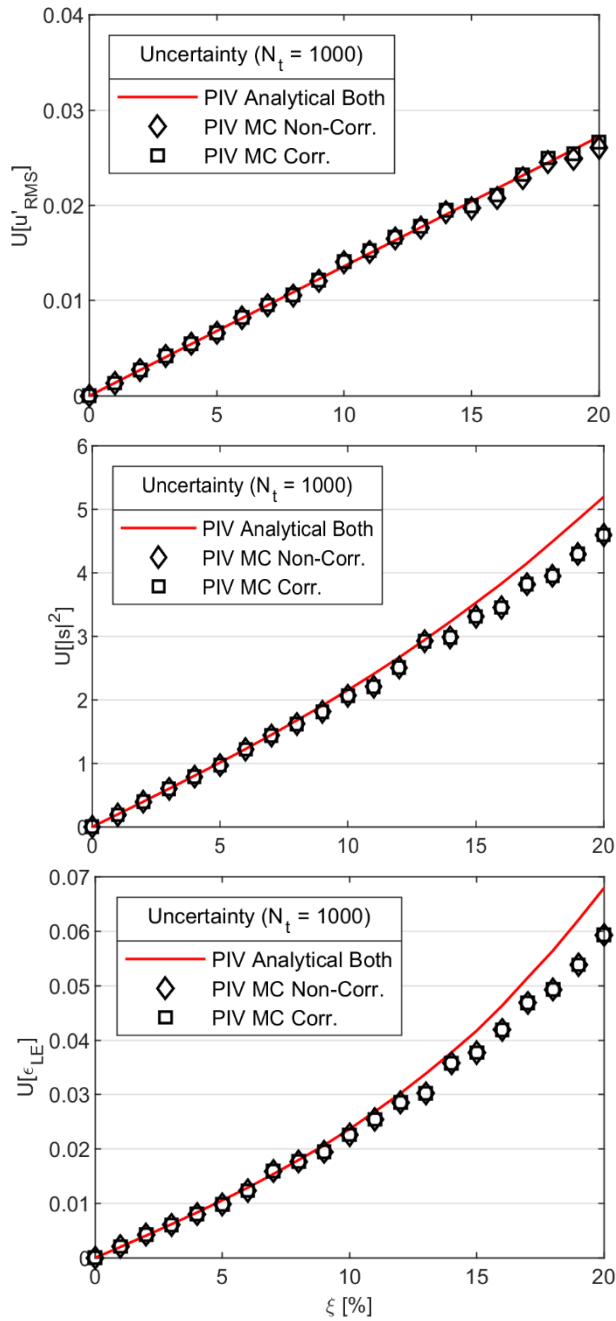


Figure 6.5 Comparison of analytical estimation and Monte-Carlo results for 95% uncertainty value ($N_{frame} = 100$, $\Delta_{IW} = 32$, 50% overlap, (32nd, 8th) sub-window) (a) velocity fluctuation RMS (b) strain rate invariant squared (c) dissipation rate

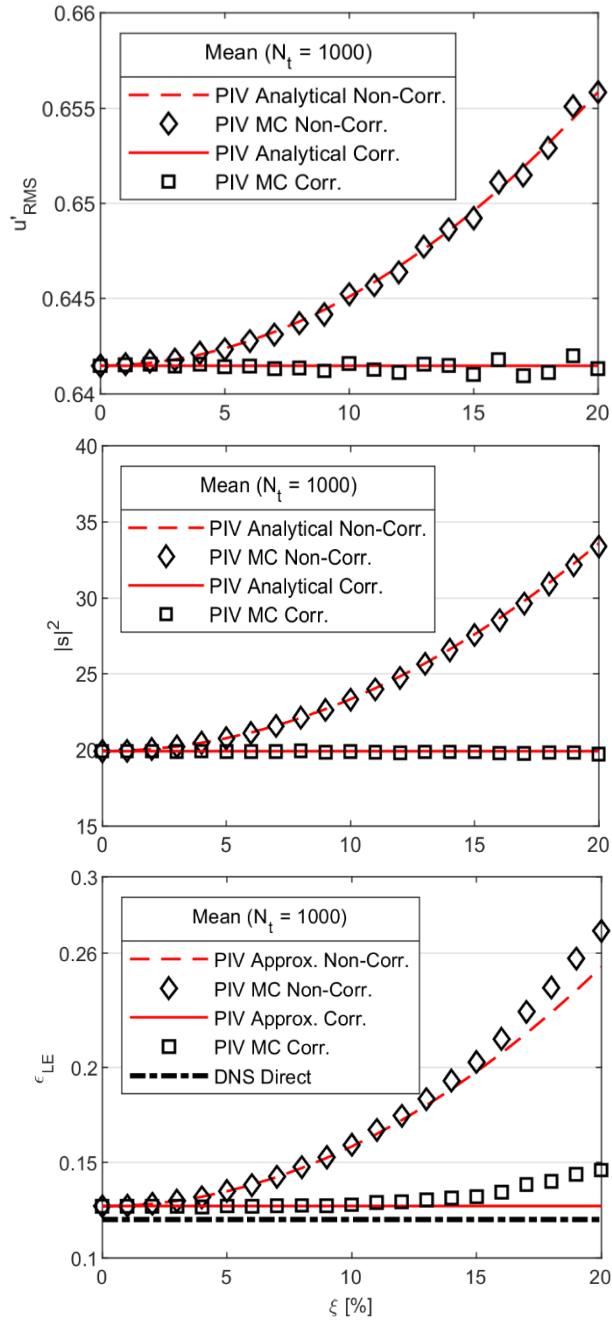


Figure 6.6 Comparison of corrected and non-corrected results for mean value ($N_{frame} = 100$, $\Delta_{IW} = 32$, 50% overlap, (32nd, 8th) sub-window) (a) velocity fluctuation RMS (b) strain rate invariant squared (c) dissipation rate

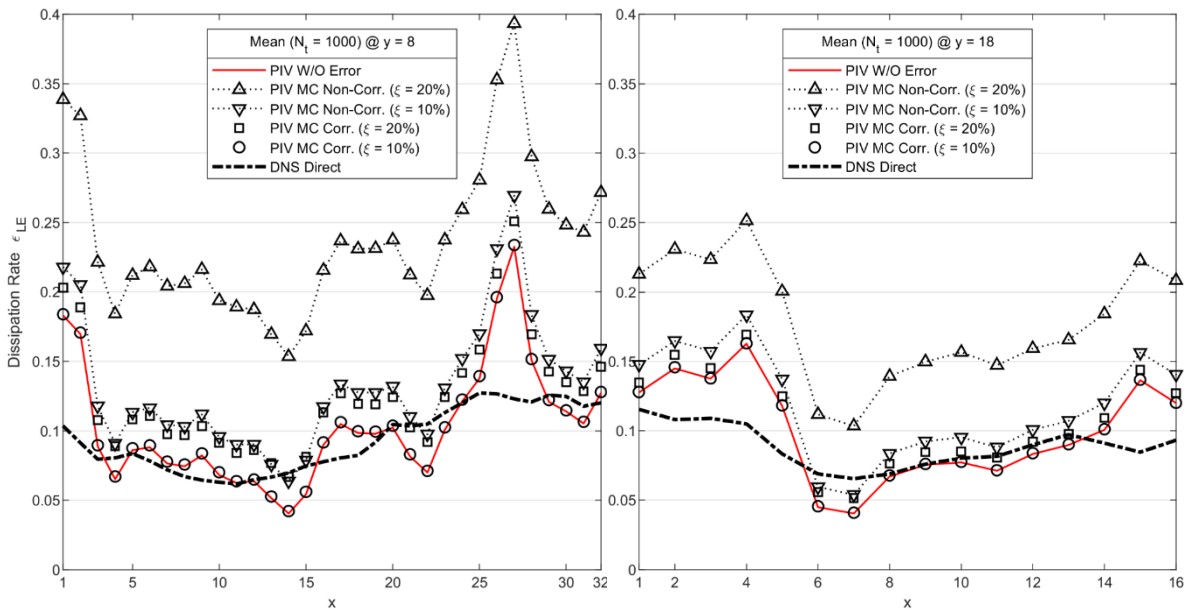


Figure 6.7 Correction to the PIV dissipation rate measurement ($N_{\text{frame}} = 100$) (a) $\Delta_{IW} = 32$, 50% overlap, $y = 8$ (b) $\Delta_{IW} = 64$, 50% overlap, $y = 18$

Chapter 7. Concluding Remarks

An experimental realization of homogeneous and isotropic turbulence (HIT) was successfully achieved in the laboratory, and the flow was quantitatively characterized using stereoscopic PIV.

From the statistically stationary homogeneous flow, ensemble, spatial- and temporal-averaging were utilized to analyze the turbulence statistics. The turbulence showed excellent homogeneity and isotropy without mean flow or mean strain, and the Taylor microscale Re_λ reached up to 228. It also manifested a skewed and sharp PDF for longitudinal velocity derivatives, indicating the dominance of vortex stretching and intermittency of dissipation. Moreover, three kinds of two-point statistics, representing flow scales, revealed scale-to-scale isotropy of the turbulence and the inertial subrange measured by the PIV setup.

The dissipation rate ε of HIT was accurately measured using three different methods, two of which utilize Kolmogorov's second similarity hypothesis: structure-function fitting and energy-spectrum fitting, whereas the other one utilizes energy balance: dissipation scaling. Furthermore, two other methods: large-eddy method and direct method were also used, which are advantageous in their applicability to general PIV experiments. In conclusion, the large-eddy method requires the PIV interrogation window size to be in the inertial subrange, while the direct method requires sufficient PIV resolution to capture the smallest fluid motions

Bibliography

- ANTONIA, R. A., DJENIDI, L. & DANAILA, L. 2014 Collapse of the turbulent dissipative range on Kolmogorov scales. *Phys. Fluids*. **26** (4), 14.
- ANTONIA, R. A., DJENIDI, L., DANAILA, L. & TANG, S. L. 2017 Small scale turbulence and the finite Reynolds number effect. *Phys. Fluids*. **29** (2), 9.
- BATCHELOR, G. K. 1953 *The theory of homogeneous turbulence*. Cambridge University Press.
- BELLANI, G. & VARIANO, E. A. 2014 Homogeneity and isotropy in a laboratory turbulent flow. *Exp. Fluids*. **55** (1), 12.
- BENEDICT, L. H. & GOULD, R. D. 1996 Towards better uncertainty estimates for turbulence statistics. *Exp. Fluids*. **22** (2), 129-136.
- BERTENS, G., VAN DER VOORT, D., BOCANEGRA-EVANS, H. & VAN DE WATER, W. 2015 Large-eddy estimate of the turbulent dissipation rate using PIV. *Exp. Fluids*. **56** (5), 9.
- BOS, W. J. T., SHAO, L. & BERTOGLIO, J. P. 2007 Spectral imbalance and the normalized dissipation rate of turbulence. *Phys. Fluids*. **19** (4), 8.
- BOS, W. J. T., CHEVILLARD, L., SCOTT, J. F. & RUBINSTEIN, R. 2012 Reynolds number effect on the velocity increment skewness in isotropic turbulence. *Phys. Fluids*. **24** (1), 21.
- CANUTO, V. M. & CHENG, Y. 1997 Determination of the Smagorinsky-Lilly constant C-s. *Phys. Fluids*. **9** (5), 1368-1378.
- CARR, Z. R., AHMED, K. A. & FORLITI, D. J. 2009 Spatially correlated precision error in digital particle image velocimetry measurements of turbulent flows. *Exp. Fluids*. **47** (1), 95-106.
- CARTER, D., PETERSEN, A., AMILI, O. & COLETTI, F. 2016 Generating and controlling homogeneous air turbulence using random jet arrays. *Exp. Fluids*. **57** (12), 15.
- CARTER, D. & COLETTI, F. 2017 Scale-to-scale anisotropy in homogeneous turbulence. *J. Fluid Mech.* **827**, 250-284.
- CHANG, K. K., BEWLEY, G. P. & BODENSCHATZ, E. 2012 Experimental study of the influence of anisotropy on the inertial scales of turbulence. *J. Fluid Mech.* **692**, 464-481.
- CHARONKO, J. J. & VLACHOS, P. P. 2013 Estimation of uncertainty bounds for individual particle image velocimetry measurements from cross-correlation peak ratio. *Meas. Sci. Technol.* **24** (6), 16.
- CHRISTENSEN, K. T. 2004 The influence of peak-locking errors on turbulence statistics computed from PIV ensembles. *Exp. Fluids*. **36** (3), 484-497.
- COLEMAN, H. W. & STEELE, W. G. 2018 *Experimentation, validation, and uncertainty analysis for engineers*. John Wiley & Sons.

- COMTE-BELLOT, G. & CORRISIN, S. 1966 Use of a contraction to improve isotropy of grid-generated turbulence. *J. Fluid Mech.* **25**, 657-682.
- DAVIDSON, P. 2015 *Turbulence: an introduction for scientists and engineers*. Oxford University Press.
- DE JONG, J., CAO, L., WOODWARD, S. H., SALAZAR, J., COLLINS, L. R. & MENG, H. 2009 Dissipation rate estimation from PIV in zero-mean isotropic turbulence. *Exp. Fluids*. **46** (3), 499-515.
- DEARDORFF, J. W. 1971 Magnitude of subgrid scale eddy coefficient. *J. Comput. Phys.* **7** (1), 120.
- DESILVA, I. P. D. & FERNANDO, H. J. S. 1994 Oscillating grids as a source of nearly isotropic turbulence. *Phys. Fluids*. **6** (7), 2455-2464.
- DJENIDI, L. & ANTONIA, R. A. 2012 A spectral chart method for estimating the mean turbulent kinetic energy dissipation rate. *Exp. Fluids*. **53** (4), 1005-1013.
- DORON, P., BERTUCCIOLI, L., KATZ, J. & OSBORN, T. R. 2001 Turbulence characteristics and dissipation estimates in the coastal ocean bottom boundary layer from PIV data. *J. Phys. Oceanogr.* **31** (8), 2108-2134.
- DOU, Z. W., PECENAK, Z. K., CAO, L. J., WOODWARD, S. H., LIANG, Z. & MENG, H. 2016 PIV measurement of high-Reynolds-number homogeneous and isotropic turbulence in an enclosed flow apparatus with fan agitation. *Meas. Sci. Technol.* **27** (3), 17.
- DOUADY, S., COUDER, Y. & BRACHET, M. E. 1991 Direct observation of the intermittency of intense vorticity filaments in turbulence. *Phys. Rev. Lett.* **67** (8), 983-986.
- ETEBARI, A. & VLACHOS, P. P. 2005 Improvements on the accuracy of derivative estimation from DPIV velocity measurements. *Exp. Fluids*. **39** (6), 1040-1050.
- FINCHAM, A. M. & SPEDDING, G. R. 1997 Low cost, high resolution DPIV for measurement of turbulent fluid flow. *Exp. Fluids*. **23** (6), 449-462.
- FOUCAUT, J. M. & STANISLAS, M. 2002 Some considerations on the accuracy and frequency response of some derivative filters applied to particle image velocimetry vector fields. *Meas. Sci. Technol.* **13** (7), 1058-1071.
- FOUCAUT, J. M., CARLIER, J. & STANISLAS, M. 2004 PIV optimization for the study of turbulent flow using spectral analysis. *Meas. Sci. Technol.* **15** (6), 1046-1058.
- FOUCAUT, J. M., CUVIER, C., STANISLAS, M. & GEORGE, W. K. 2016 Quantification of the Full Dissipation Tensor from an L-Shaped SPIV Experiment in the Near Wall Region. *Progress in Wall Turbulence 2*. Cham: Springer.429-439.
- FRIEDMAN, P. D. & KATZ, J. 2002 Mean rise rate of droplets in isotropic turbulence. *Phys. Fluids*. **14** (9), 3059-3073.
- GERMANO, M., PIOMELLI, U., MOIN, P. & CABOT, W. H. 1991 A dynamic subgrid-scale eddy viscosity model. *Physics of Fluids A-Fluid Dynamics*. **3** (7), 1760-1765.

- GERMANO, M. 1992 Turbulence - the filtering approach. *J. Fluid Mech.* **238**, 325-336.
- GOEPFERT, C., MARIE, J. L., CHAREYRON, D. & LANCE, M. 2010 Characterization of a system generating a homogeneous isotropic turbulence field by free synthetic jets. *Exp. Fluids.* **48** (5), 809-822.
- GOTOH, T., FUKAYAMA, D. & NAKANO, T. 2002 Velocity field statistics in homogeneous steady turbulence obtained using a high-resolution direct numerical simulation. *Phys. Fluids.* **14** (3), 1065-1081.
- GRAYSON, K., DE SILVA, C. M., HUTCHINS, N. & MARUSIC, I. 2018 Impact of mismatched and misaligned laser light sheet profiles on PIV performance. *Exp. Fluids.* **59** (1), 15.
- HUANG, H., DABIRI, D. & GHARIB, M. 1997 On errors of digital particle image velocimetry. *Meas. Sci. Technol.* **8** (12), 1427-1440.
- HWANG, W. & EATON, J. K. 2004 Creating homogeneous and isotropic turbulence without a mean flow. *Exp. Fluids.* **36** (3), 444-454.
- ISHIHARA, T., GOTOH, T. & KANEDA, Y. 2009 Study of High-Reynolds Number Isotropic Turbulence by Direct Numerical Simulation. *Annu. Rev. Fluid Mech.* **41**, 165-180.
- JUNG, H., LEE, H. & HWANG, W. 2019 Denoising PIV velocity fields and improving vortex identification using spatial filters. *J. Kor. Soc. Vis.* **17** (2), 48-57.
- KAHLER, C. J., SCHARNOWSKI, S. & CIERPKA, C. 2012 On the resolution limit of digital particle image velocimetry. *Exp. Fluids.* **52** (6), 1629-1639.
- KAHLER, C. J., ASTARITA, T., VLACHOS, P. P., SAKAKIBARA, J., HAIN, R., DISCETTI, S., . . . CIERPKA, C. 2016 Main results of the 4th International PIV Challenge. *Exp. Fluids.* **57** (6), 71.
- KANEDA, Y., ISHIHARA, T., YOKOKAWA, M., ITAKURA, K. & UNO, A. 2003 Energy dissipation rate and energy spectrum in high resolution direct numerical simulations of turbulence in a periodic box. *Phys. Fluids.* **15** (2), L21-L24.
- KOLMOGOROV, A. N. 1941a The local structure of turbulence in incompressible viscous fluid for very large Reynolds numbers. *Dokl. Akad. Nauk SSSR.* **30** (4), 301-305. [English translation by Levin, V. 1991 *Proc. R. Soc. Lond. A.* **434**, 9-13.]
- KOLMOGOROV, A. N. 1941b Dissipation of energy in the locally isotropic turbulence. *Dokl. Akad. Nauk SSSR.* **32** (1), 16-18. [English translation by Levin, V. 1991 *Proc. R. Soc. Lond. A.* **434**, 15-17.]
- KOLMOGOROV, A. N. 1962 A refinement of previous hypotheses concerning the local structure of turbulence in a viscous incompressible fluid at high Reynolds number. *J. Fluid Mech.* **13** (1), 82-85.
- KRAICHNAN, R. H. 1974 On Kolmogorov's inertial-range theories. *J. Fluid Mech.* **62**, 305-330.
- LAVOIE, P., AVALLONE, G., DE GREGORIO, F., ROMANO, G. P. & ANTONIA, R. A. 2007 Spatial resolution of PIV for the measurement of turbulence. *Exp. Fluids.* **43** (1), 39-51.

- LEE, H. & HWANG, W. 2019 Error quantification of 3D homogeneous and isotropic turbulence measurements using 2D PIV. *Int. J. Heat Fluid Flow*. **78**, 12.
- LI, D. X., MUSTE, M. & WANG, X. K. 2008 Quantification of the bias error induced by velocity gradients. *Meas. Sci. Technol.* **19** (1), 7.
- LI, Y., PERLMAN, E., WAN, M. P., YANG, Y. K., MENEVEAU, C., BURNS, R., . . . EYINK, G. 2008 A public turbulence database cluster and applications to study Lagrangian evolution of velocity increments in turbulence. *J. Turbul.* **9** (31), 1-29.
- LILLY, D. K. 1992 A proposed modification of the Germano-subgrid-scale closure method. *Physics of Fluids A-Fluid Dynamics*. **4** (3), 633-635.
- LILLY, K. 1966 On the application of the eddy viscosity concept in the inertial sub-range of turbulence. *NCAR, Manuscript*. No. 123.
- LIU, S. W., MENEVEAU, C. & KATZ, J. 1994 On the properties of similarity subgrid-scale models as deduced from measurements in a turbulent jet. *J. Fluid Mech.* **275**, 83-119.
- LIU, S. W., KATZ, J. & MENEVEAU, C. 1999 Evolution and modelling of subgrid scales during rapid straining of turbulence. *J. Fluid Mech.* **387**, 281-320.
- LOURENCO, L. & KROTHAPALLI, A. 1995 On the accuracy of velocity and vorticity measurements with PIV. *Exp. Fluids*. **18** (6), 421-428.
- LUMLEY, J. L. 1992 Some comments on turbulence. *Physics of Fluids A-Fluid Dynamics*. **4** (2), 203-211.
- MAZELLIER, N. & VASSILICOS, J. C. 2008 The turbulence dissipation constant is not universal because of its universal dependence on large-scale flow topology. *Phys. Fluids*. **20** (1), 9.
- MCCOMB, W. D., BERERA, A., SALEWSKI, M. & YOFFE, S. 2010 Taylor's (1935) dissipation surrogate reinterpreted. *Phys. Fluids*. **22** (6), 4.
- MENEVEAU, C. & LUND, T. S. 1997 The dynamic Smagorinsky model and scale-dependent coefficients in the viscous range of turbulence. *Phys. Fluids*. **9** (12), 3932-3934.
- MENEVEAU, C. & KATZ, J. 2000 Scale-invariance and turbulence models for large-eddy simulation. *Annu. Rev. Fluid Mech.* **32**, 1-32.
- MEUNIER, P. & LEWEKE, T. 2003 Analysis and treatment of errors due to high velocity gradients in particle image velocimetry. *Exp. Fluids*. **35** (5), 408-421.
- MONIN, A. S. & YAGLOM, A. M. 1971 *Statistical fluid mechanics : mechanics of turbulence*. MIT Press.
- MOURI, H., TAKAOKA, M., HORI, A. & KAWASHIMA, Y. 2002 Probability density function of turbulent velocity fluctuations. *Phys. Rev. E*. **65** (5), 7.
- NOBACH, H. & HONKANEN, M. 2005 Two-dimensional Gaussian regression for sub-pixel displacement estimation in particle image velocimetry or particle position estimation in particle tracking velocimetry. *Exp. Fluids*. **38** (4), 511-515.

- NOBACH, H. & BODENSCHATZ, E. 2009 Limitations of accuracy in PIV due to individual variations of particle image intensities. *Exp. Fluids*. **47** (1), 27-38.
- OTT, S. & MANN, J. 2000 An experimental investigation of the relative diffusion of particle pairs in three-dimensional turbulent flow. *J. Fluid Mech.* **422**, 207-223.
- PEARSON, B. R. & ANTONIA, R. A. 2001 Reynolds-number dependence of turbulent velocity and pressure increments. *J. Fluid Mech.* **444**, 343-382.
- PEARSON, B. R., KROGSTAD, P. A. & VAN DE WATER, W. 2002 Measurements of the turbulent energy dissipation rate. *Phys. Fluids*. **14** (3), 1288-1290.
- PRASAD, A. K. & JENSEN, K. 1995 Scheimpflug stereocamera for particle image velocimetry in liquid flows. *Appl. Optics*. **34** (30), 7092-7099.
- REUSS, D. L., MEGERLE, M. & SICK, V. 2002 Particle-image velocimetry measurement errors when imaging through a transparent engine cylinder. *Meas. Sci. Technol.* **13** (7), 1029-1035.
- ROESGEN, T. 2003 Optimal subpixel interpolation in particle image velocimetry. *Exp. Fluids*. **35** (3), 252-256.
- SAARENINNE, P. & PIIRTO, M. 2000 Turbulent kinetic energy dissipation rate estimation from PIV velocity vector fields. *Exp. Fluids*. **29**, S300-S307.
- SAARENINNE, P., PIIRTO, M. & ELORANTA, H. 2001 Experiences of turbulence measurement with PIV. *Meas. Sci. Technol.* **12** (11), 1904-1910.
- SADDOUGHI, S. G. & VEERAVALLI, S. V. 1994 Local isotropy in turbulent boundary-layers at high Reynolds-number. *J. Fluid Mech.* **268**, 333-372.
- SCHARNOWSKI, S. & KAHLER, C. J. 2016a Estimation and optimization of loss-of-pair uncertainties based on PIV correlation functions. *Exp. Fluids*. **57** (2), 11.
- SCHARNOWSKI, S. & KAHLER, C. J. 2016b On the loss-of-correlation due to PIV image noise. *Exp. Fluids*. **57** (7), 12.
- SCHARNOWSKI, S., BROSS, M. & KAHLER, C. J. 2019 Accurate turbulence level estimations using PIV/PTV. *Exp. Fluids*. **60** (1), 12.
- SCIACCHITANO, A., WIENEKE, B. & SCARANO, F. 2013 PIV uncertainty quantification by image matching. *Meas. Sci. Technol.* **24** (4), 16.
- SCIACCHITANO, A., NEAL, D. R., SMITH, B. L., WARNER, S. O., VLACHOS, P. P., WIENEKE, B. & SCARANO, F. 2015 Collaborative framework for PIV uncertainty quantification: comparative assessment of methods. *Meas. Sci. Technol.* **26** (7), 16.
- SCIACCHITANO, A. & WIENEKE, B. 2016 PIV uncertainty propagation. *Meas. Sci. Technol.* **27** (8), 16.
- SCIACCHITANO, A. 2019 Uncertainty quantification in particle image velocimetry. *Meas. Sci. Technol.* **30** (9), 31.
- SHENG, J., MENG, H. & FOX, R. O. 2000 A large eddy PIV method for turbulence dissipation rate estimation. *Chem. Eng. Sci.* **55** (20), 4423-4434.
- SMAGORINSKY, J. 1963 General circulation experiments with the primitive equations. *Monthly Weather Review*. **91** (3), 99-164.

- SOLOFF, S. M., ADRIAN, R. J. & LIU, Z. C. 1997 Distortion compensation for generalized stereoscopic particle image velocimetry. *Meas. Sci. Technol.* **8** (12), 1441-1454.
- SREENIVASAN, K. R. 1984 On the scaling of the turbulence energy dissipation rate. *Phys. Fluids.* **27** (5), 1048-1051.
- SREENIVASAN, K. R. 1995 On the universality of the Kolmogorov constant. *Phys. Fluids.* **7** (11), 2778-2784.
- SREENIVASAN, K. R. & ANTONIA, R. A. 1997 The phenomenology of small-scale turbulence. *Annu. Rev. Fluid Mech.* **29**, 435-472.
- SREENIVASAN, K. R. 1998 An update on the energy dissipation rate in isotropic turbulence. *Phys. Fluids.* **10** (2), 528-529.
- TANAKA, T. & EATON, J. K. 2007 A correction method for measuring turbulence kinetic energy dissipation rate by PIV. *Exp. Fluids.* **42** (6), 893-902.
- TAVOULARIS, S., BENNETT, J. C. & CORRISIN, S. 1978 Velocity derivative skewness in small Reynolds number, nearly isotropic turbulence. *J. Fluid Mech.* **88**, 63-69.
- TAYLOR, G. I. 1935 Statistical theory of turbulence. *Proc. R. Soc. Lond. A-Math. Phys. Sci.* **151** (A873), 421-444.
- THORMANN, A. & MENEVEAU, C. 2014 Decay of homogeneous, nearly isotropic turbulence behind active fractal grids. *Phys. Fluids.* **26** (2), 28.
- TIMMINS, B. H., WILSON, B. W., SMITH, B. L. & VLACHOS, P. P. 2012 A method for automatic estimation of instantaneous local uncertainty in particle image velocimetry measurements. *Exp. Fluids.* **53** (4), 1133-1147.
- VAN DOORNE, C. W. H. & WESTERWEEL, J. 2007 Measurement of laminar, transitional and turbulent pipe flow using Stereoscopic-PIV. *Exp. Fluids.* **42** (2), 259-279.
- VARIANO, E. A., BODENSCHATZ, E. & COWEN, E. A. 2004 A random synthetic jet array driven turbulence tank. *Exp. Fluids.* **37** (4), 613-615.
- VASSILICOS, J. C. 2015 Dissipation in Turbulent Flows. *Annu. Rev. Fluid Mech.* **47**, 95-114.
- VINCENT, A. & MENEGUZZI, M. 1991 The spatial structure and statistical properties of homogeneous turbulence. *J. Fluid Mech.* **225**, 1-20.
- VON KARMAN, T. & HOWARTH, L. 1937 On the statistical theory of turbulence. *Proc. Natl. Acad. Sci. U. S. A.* **23**, 98-105.
- WANG, L. P., CHEN, S. Y., BRASSEUR, J. G. & WYNGAARD, J. C. 1996 Examination of hypotheses in the Kolmogorov refined turbulence theory through high-resolution simulations .1. Velocity field. *J. Fluid Mech.* **309**, 113-156.
- WESTERWEEL, J. 1994 Efficient detection of spurious vectors in particle image velocimetry data. *Exp. Fluids.* **16** (3-4), 236-247.
- WESTERWEEL, J. 2000 Theoretical analysis of the measurement precision in particle image velocimetry. *Exp. Fluids.* **29**, S3-S12.
- WESTERWEEL, J. & SCARANO, F. 2005 Universal outlier detection for PIV data. *Exp. Fluids.* **39** (6), 1096-1100.

- WESTERWEEL, J. 2008 On velocity gradients in PIV interrogation. *Exp. Fluids*. **44** (5), 831-842.
- WIENEKE, B. 2015 PIV uncertainty quantification from correlation statistics. *Meas. Sci. Technol.* **26** (7), 10.
- WILSON, B. M. & SMITH, B. L. 2013a Taylor-series and Monte-Carlo-method uncertainty estimation of the width of a probability distribution based on varying bias and random error. *Meas. Sci. Technol.* **24** (3), 11.
- WILSON, B. M. & SMITH, B. L. 2013b Uncertainty on PIV mean and fluctuating velocity due to bias and random errors. *Meas. Sci. Technol.* **24** (3), 15.
- YEUNG, P. K. & ZHOU, Y. 1997 Universality of the Kolmogorov constant in numerical simulations of turbulence. *Phys. Rev. E*. **56** (2), 1746-1752.
- ZARIPOV, D., LI, R. F. & DUSHIN, N. 2019 Dissipation rate estimation in the turbulent boundary layer using high-speed planar particle image velocimetry. *Exp. Fluids*. **60** (1), 16.
- ZIMMERMANN, R., XU, H. T., GASTEUIL, Y., BOURGOIN, M., VOLK, R., PINTON, J. F. & BODENSCHATZ, E. 2010 The Lagrangian exploration module: An apparatus for the study of statistically homogeneous and isotropic turbulence. *Rev. Sci. Instrum.* **81** (5), 8.

국문 초록

난류 현상을 이해하는 데 기초가 되는 균질한 등방성 난류를 실험적으로 구현하고 통계적인 방법으로 분석하였다. 합성 제트 발생기로 구성된 난류 상자 중앙부에 평균 유동과 평균 기울기가 없는 균질한 등방성 난류가 생성되었으며, 스테레오 입자영상유속계를 이용하여 평면 계측영역의 세 방향 속도 성분을 계측하였다. 정상 상태의 균질한 유동장을 독립적으로 측정함으로써 각 속도 벡터를 시공간 전체에 대한 통계적 표본으로 간주하고 단일점 통계치와 이점 간 통계치를 추계하였다. 단일점 통계치를 분석함으로써 난류 유동의 정상성, 균질성, 등방성이 충분함을 확인하였다. 속도 상관 함수, 속도 구조 함수, 에너지 스펙트럼을 포함하는 이점 간 통계치를 분석함으로써 다규모 등방성과 관성 영역에서의 상사성 등을 확인하였다. 난류 소산율을 측정하는 총 다섯 가지 방법을 비교분석함으로써 각 방법의 성능을 평가하고 입자영상유속계로 난류를 측정하는 일반적인 상황에서의 필요조건을 검토하였다. 관성 영역에서의 난류의 보편성에 기초한 측정법과 규모 간 에너지 균형에 기초한 측정법은 일관된 결과를 보였으며, 따라서 이를 본 실험에 대한 정확한 계측값으로서 활용하였다. 반면에 균질한 등방성 난류뿐만 아니라 일반적인 난류 조건에 적용 가능한 큰 에디 방법과 직접 측정 방법은 각각 계측의 공간 분해능이 과하거나(관성영역보다 작은 영역을 분해하는 경우) 부족하여(유체의 가장 작은 규모 움직임을 포착하지 못하는 경우) 난류 소산율을 과소 측정할 수 있음을 확인하였다. 따라서 입자영상유속계를 이용한 난류 측정 실험에서는 이 조건이 충족되도록 계측영역과 상관창 크기를 통제하여야 한다.

주요어: 균질한 등방성 난류, 난류 통계치, 소산율 측정,
스테레오 입자영상유속계

학 번: 2018-27421